NASA

MEMORANDUM

HEAT-TRANSFER MEASUREMENTS ON A 5.5-INCH-DIAMETER

HEMISPHERICAL CONCAVE NOSE IN FREE FLIGHT

AT MACH NUMBERS UP TO 6.6

By Jack Levine and Charles B. Rumsey

Langley Research Center
Langley Field, Va.

CASE FILE COPY

NATIONAL AERONAUTICS AND SPACE ADMINISTRATION
WASHINGTON
December 1958

NATIONAL AERONAUTICS AND SPACE ADMINISTRATION

MEMORANDUM 10-21-58L

HEAT-TRANSFER MEASUREMENTS ON A 5.5-INCH-DIAMETER

HEMISPHERICAL CONCAVE NOSE IN FREE FLIGHT

AT MACH NUMBERS UP TO 6.6[*]

By Jack Levine and Charles B. Rumsey

SUMMARY

The aerodynamic heat transfer to a hemispherical concave nose has been measured in free flight at Mach numbers from 3.5 to 6.6 with corresponding Reynolds numbers based on nose diameter from 7.4×10^6 to 14×10^6.

Over the test Mach number range the heating on the cup nose, expressed as a ratio to the theoretical stagnation-point heating on a hemisphere nose of the same diameter, varied from 0.05 to 0.13 at the stagnation point of the cup, was approximately 0.1 at other locations within $40°$ of the stagnation point, and varied from 0.6 to 0.8 just inside the lip where the highest heating rates occurred. At a Mach number of 5 the total heat input integrated over the surface of the cup nose including the lip was 0.55 times the theoretical value for a hemisphere nose with laminar boundary layer and 0.76 times that for a flat face.

The heating at the stagnation point was approximately 1/5 as great as steady-flow tunnel results. Extremely high heating rates at the stagnation point (on the order of 30 times the stagnation-point values of the present test), which have occurred in conjunction with unsteady oscillatory flow around cup noses in wind-tunnel tests at Mach and Reynolds numbers within the present test range, were not observed.

INTRODUCTION

At hypersonic flight speeds bodies generally must be blunt nosed to some extent in order to reduce the heat-transfer rates to manageable proportions. The Langley Pilotless Aircraft Research Division is

_____

[*]Title, Unclassified.

conducting a program to investigate the heat-transfer characteristics of various blunt-nose shapes by use of rocket-model and preflight-jet tests. Results of some of these investigations are reported in references 1 to 3, which present heat-transfer results of flight tests on a 1/10-power nose and a flat face, and preflight-jet tests on six blunt noses.

In the present investigation, the aerodynamic heating on a hemispherical concave nose was measured. This test and a preflight-jet test of a similar model, reported in reference 4, were initiated on the basis of some exploratory tests which indicated low heating rates at the stagnation point of concave noses (ref. 5). The purpose of the present test was to make a more detailed investigation of heating over this nose shape under free-flight conditions.

A preliminary analysis of the present data showed heating rates within the cup nose which were surprisingly lower than the preflight-jet data of reference 4, and as a result several wind-tunnel investigations were initiated and rushed to completion. A summary of cup-nose heating data, including preliminary data from the present test, data from the preflight-jet test of reference 4, data from the wind-tunnel facilities of the Langley Gas Dynamics Branch (ref. 6), and unpublished data from the Langley Unitary Plan wind tunnel, is given in reference 7. Although it is not particularly apparent from the summary of the cup-nose data given in reference 7, the data from the present flight test are considerably lower than results obtained in the various wind tunnels, as will be discussed in this report, and the inconsistency is as yet unresolved.

The present flight test was made with a two-stage propulsion system consisting of a Nike booster and a Recruit sustainer motor which was made available by the U. S. Air Force. The test vehicle attained a maximum Mach number of 6.7. The test Reynolds numbers based on the 5.47-inch diameter of the nose ranged from 7.4×10^6 to 14×10^6 for the corresponding Mach number range from 3.5 to 6.64.

The flight test was conducted at the Langley Pilotless Aircraft Research Station at Wallops Island, Va., in October 1957.

SYMBOLS

A_{n+1} cross-sectional area between elements n and $n + 1$

A_{n-1} cross-sectional area between elements n and $n - 1$

N_{St} Stanton number, $h/c_p \rho V_g$

c_p specific heat of air at constant pressure, Btu/(lb)(°F)

D   diameter of nose, ft

g   acceleration due to gravity, 32.2 ft/sec^2

h   local aerodynamic heat-transfer coefficient, Btu/(sec)(sq ft)(°F)

k   conductivity of wall material, Btu/(sec)(sq ft)(°F/ft)

M   Mach number

p   pressure, lb/sq in.

$p_{t,2}$ total pressure downstream of a normal shock, lb/sq in.

q   heating rate, Btu/(sec)(sq ft)

r   radius, in.

R   Reynolds number

$R_{\infty,D}$ free-stream Reynolds number based on nose diameter, $\rho_\infty V_\infty D/\mu_\infty$

η temperature-recovery factor (held constant at 0.85)

s   distance along surface of nose from stagnation point to center of lip

S_n area of element n exposed to air flow, sq ft

T   temperature, °R unless otherwise noted

T_t stagnation temperature, °R

t   time, sec

V   velocity, ft/sec

a   speed of sound, ft/sec

x   distance along surface of nose from stagnation point

Δx_{n+1} distance between thermocouple locations in elements n and n + 1, ft

Δx_{n-1} distance between thermocouple locations in elements n and $n - 1$, ft

α angle of attack, deg

ρ density of air, slugs/cu ft

σ Stefan-Boltzmann constant, $Btu/(sec)(sq\ ft)(^\circ R)^4$

μ absolute viscosity of air, slugs/ft-sec

Subscripts:

aw   adiabatic wall

th   theoretical

l local conditions, just outside boundary layer

o   at stagnation point

w   at wall

∞ undisturbed free stream ahead of model

MODEL, INSTRUMENTATION, AND TEST TECHNIQUE

Model

The general model arrangement and pertinent dimensions are shown in figure 1(a). A photograph of the model is shown in figure 1(b). The model consisted of the test nose and an instrument section mounted on the thrust face of a Recruit rocket motor. The test nose was a cylinder with a hemispherically concave face. It was attached to a short conical section of 40° total angle which was mounted on the forward end of the instrumentation section.

The test nose was spun from Inconel and varied in thickness from 0.043 to 0.064 inch. The measured skin thickness at the temperature-measuring stations is presented in figure 2(a). Figure 2(a) also shows the dimensions of the test nose and the locations of the thermocouples and a pressure orifice. No backing material was used under the skin of the nose in order that the skin temperatures would not be influenced by heat sinks. The instrumentation was protected from the internal radiation of the nose skin by a thick-walled steel radiation shield mounted inside the nose. A photograph of the nose and instrumentation section is shown in figure 2(b).

The maximum surface roughness of the nose was 30 microinches. This nose was not given the superpolished finish of the nose used in the investigation of reference 1.

Stabilization of the model was achieved by means of a conical frustum having a total angle of 20° which was attached to the rear of the model.

The model was boosted by a fin-stabilized Nike (M5 JATO) rocket motor. A photograph of the model and booster on the launcher is shown in figure 3.

Instrumentation

The model was equipped with six channels of telemetering. One channel transmitted pressure, three transmitted accelerations (longitudinal, transverse, and normal), and two transmitted temperatures. The voltage output of the 16 thermocouples was commutated on the two temperature channels. The commutation arrangement was such that data from eight thermocouples were recorded approximately every 0.1 second and data from the remaining eight were recorded approximately every 0.2 second. Three standard voltages were also commutated on each temperature channel approximately every 0.2 second. These voltages, supplied by a mercury cell and voltage dividing network, were chosen to correspond to the lowest, mean, and highest skin temperatures expected during the test, and provided an in-flight calibration of the complete thermocouple telemetering system.

The thermocouples, made of No. 30 (0.010-inch-diameter) chromel-alumel wire, were spotwelded to the inner surface of the Inconel skin at the stations indicated in figure 2(a).

The longitudinal accelerometer was calibrated to cover the range from 140g (thrust acceleration) to -70g (drag deceleration) and was included to provide velocity information in case of radar failure. The normal and transverse accelerometers were calibrated to cover the range from 25g to -25g.

The pressure orifice was located at the most forward portion of the lip of the nose as shown in figure 2(a). The pressure gage was calibrated from 4 to 100 lb/sq in. abs.

In addition to the instrumentation carried internally, the model was tracked by a CW Doppler velocimeter and an NACA modified SCR-584 radar set to provide velocity and trajectory data, respectively. Atmospheric and wind conditions were determined by means of a radiosonde launched near the time of flight and tracked by a Rawin set AN/GMD-1A.

difference between outside and inside temperatures. This assumption is correct for a linear increase in heating rate with time. The method used to compute the lateral heat-flow rates from these lateral temperature distributions was similar to that used in reference 2. The nose was divided into concentric rings, one for each thermocouple location, and the temperature of each ring was assumed to be the average temperature at the thermocouple location. The lateral heat-flow rates were then computed for ring n by the equation

$$q_{n,\text{lateral}} = \frac{kA_{n-1}\left(T_n - T_{n-1}\right)}{S_n \, \Delta x_{n-1}} + \frac{kA_{n+1}\left(T_n - T_{n+1}\right)}{S_n \, \Delta x_{n+1}} \tag{2}$$

where $q_{n,\text{lateral}}$ is the resultant conductive heat flow into ring n, and is given in $Btu/(sec)(sq\ ft)$. The contact areas A_{n-1} and A_{n+1}, the lengths Δx_{n-1} and Δx_{n+1} to the adjacent thermocouples, and the area of the ring exposed to the air flow S_n were determined from the dimensions of the nose and rings. The sizes of the rings were chosen so that the distance between thermocouples was equally divided, and the dividing surface was in each case taken perpendicular to the outside surface of the skin. This finite-difference method, although only an approximation, is believed to be the best means available for computing the lateral heat-flow rates from the rather widely spaced skin-temperature measurements. The lateral heat-flow rates were small (less than 15 percent of the aerodynamic heating rates) until about 2 seconds after peak Mach number (when $M_{\infty} \approx 4.5$), except for the locations near the lip. Because of the large temperature gradients along the skin near the lip, the lateral heat-flow rates were larger for thermocouples 5 through 9, being as large as 50 percent of the aerodynamic heating rates at station 8 at a time of 7.44 seconds (M = 5.5) when the model was slowing up and the heating rates were small.

Heat losses from the skin due to radiation were computed and found to be entirely negligible during the high-speed portion of the flight. However, during the terminal portion of the final coast (when the Mach number had decreased below about 4.5) the skin was hot and the aerodynamic heating rates were becoming small so that radiation was significant relative to the aerodynamic heating. For this terminal portion of the final coast, the heat-flow rates due to external radiation were computed from

$$q_{\text{radiation}} = \epsilon\sigma T_w^{4} \tag{3}$$

where ϵ, the emissivity of polished Inconel, was obtained from reference 9. Internal radiation was not included in this computation since most of the area to which the interior surface of the skin can radiate is at elevated temperatures.

The experimental aerodynamic heat-transfer rates shown in figure 8 were determined by adding algebraically the lateral heat-flow rates for each station and the external radiation rates, when applicable, to the corresponding one-dimensional heat-flow rates.

Aerodynamic heat-transfer coefficients were computed from the experimental heat-transfer rates by use of the equation

$$h = \frac{q_{aero}}{T_{aw} - T_w} \tag{4}$$

Values of T_{aw} were obtained from the relation

$$T_{aw} = \eta \left(T_t - T_l \right) + T_l \tag{5}$$

A value of 0.85 was assumed for the recovery factor, and T_t was determined from flight conditions and perfect gas relations. (See fig. 4(c).) The local temperatures at the measurement stations were determined by use of the pressure distribution for this nose shape at a Mach number of 2, reported in reference 4 and shown in figure 9. (It should be noted that the fairing of the pressure distribution reported in reference 4 was somewhat arbitrary because there were too few pressure pickups in the vicinity of the lip.)

Values of Stanton number based on free-stream conditions were computed from

$$N_{St,\infty} = \frac{h}{g c_p \rho_\infty V_\infty} \tag{6}$$

where the specific heat of air c_p is taken as a constant of 0.24.

ACCURACY

The measured temperatures are believed to be accurate within ±1 per-cent of the full-scale range of the thermocouple instrumentation. There-fore, the skin-temperature measurements are accurate within ±20° F.

The pressure measurements are believed to be accurate within ±2 per-cent of the full-scale range of the pressure gage. This results in an accuracy in $p_l/p_{t,2}$ of ±0.02 at the low Mach numbers (e.g., $M_\infty = 2.5$) to ±0.005 at the high Mach numbers (e.g., $M_\infty = 5.6$).

The velocity data, which were obtained from Doppler radar, are believed to be accurate within ±5 ft/sec. This, along with radiosonde and SCR-584 tracking radar accuracy, results in a possible error in Mach number of about ±0.01.

RESULTS AND DISCUSSION

Temperature and Heating-Rate Measurements

The time histories of outside wall temperature for several of the measurement stations are plotted in figure 7 and indicate the general pattern of heating over the nose surface. The temperatures increased slowly at the stagnation point as compared with the lip locations. The most rapid temperature increases occurred at the location just inside the lip. On the cylinder immediately behind the lip the temperatures were very low, probably indicating an overexpansion of the flow, while farther back along the cylinder the temperatures were comparable to those on the lip.

The experimental heating rates for the 11 in-line stations along the nose are shown in figure 8. The data points, which are shown only for locations 1 and 6a (figs. 8(a) and 8(c)) are the heating rates com-puted from the skin-temperature time histories by the one-dimensional method as described in the section entitled "Data Reduction" and are not corrected for conduction and radiation; the aerodynamic heating rates (one-dimensional values corrected for conduction and radiation) are shown by the solid curves. The one-dimensional rates for stations 1 and 6a are included to indicate the magnitude of the corrections. At station 1 the corrections were very small; at station 6a, which had the largest con-duction correction, they were relatively very large after about 7.5 sec-onds ($M_\infty < 5.4$). Also, these points typify the time spacing and the scatter of the one-dimensional heating-rate data.

The aerodynamic heating rates were very similar at locations within $40°$ of the center point of the cup, that is, at stations 1, 2, and 3a. The rates were progressively higher at locations farther from the center point, with the maximum rate of 280 Btu/(sec)(sq ft) occurring at station 6a just inside the lip. Station 9, on the cylinder behind the lip, had the lowest heating rates and reached only 31 Btu/(sec)(sq ft).

Pressure Measurements

The pressure distribution of reference 4 for $M_\infty = 2$ and $\alpha = 0°$ is shown in figure 9, together with the pressure measurements obtained on the lip of the nose in the present test for Mach numbers of 2.5 to 5.6. Pressure data were not obtained at Mach numbers higher than 5.6 or during the coast after maximum Mach number because the pressures exceeded the range of the instrument, and the gage appeared to have been damaged while off scale.

The data shown for the present test in figure 9 represent lip pressures p_l from 22 to 97 lb/sq in. abs, which were divided by the theoretical total pressure behind a normal shock $p_{t,2}$. These data appear to indicate a slight increase in lip pressure ratio with increasing Mach number, but are all in fair agreement with the data for a Mach number of 2 from reference 4.

It may also be noted that in the test of reference 4, a low pressure region existed on the cylinder behind the lip at station $x/s = 1.18$, which corresponds with the low heating experienced in the present test at station 9 $(x/s = 1.16)$.

For lack of further knowledge and since the lip measurements were in fair agreement, the distribution and fairing of reference 4 were used to compute the local flow conditions around the nose in the reduction of the present heat-transfer data.

Heat Transfer

The experimental heat-transfer coefficients for the stations in the cup and on the lip, determined as indicated in the section entitled "Data Reduction," are shown in figure 10 plotted against Mach number. The data are shown as ratios of the theoretical heat-transfer coefficient at the stagnation point of a 5.47-inch-diameter hemisphere with the same stagnation-point skin temperature as station 1 on the cup nose. The theory is that of Fay and Riddell (eq. (63), of ref. 10), with the assumption of Lewis number of 1, Prandtl number of 0.71, Sutherland viscosity law, and perfect gas relations for density, stagnation temperature, and

enthalpy. The required values of dV/dx were obtained from a plot presented in reference 2.

Figure 10 shows that the heat-transfer coefficient at the center point of the cup nose was only 0.05 of the theoretical hemisphere stagnation-point value at $M_\infty = 4$ and increased to 0.13 as M_∞ increased to 6.6.

The ratios of $h/h_{0,th}$ are approximately 0.1 for stations 2 and 3, which are within $40°$ of the stagnation point. These data show a smaller variation with Mach number than the data for station 1. The ratios are increasingly higher at stations 4 and 5 and remain fairly constant with Mach number. The highest ratios of $h/h_{0,th}$ are shown for station 6a just inside the lip, where a value of 0.8 was reached. The lip location, station 7a, reached a maximum ratio $h/h_{0,th}$ of 0.7.

The duplication of the ratios $h/h_{0,th}$ at station 1 for increasing and decreasing Mach number indicates that the Reynolds number effect at this station was negligible over the range of the test. At a Mach number of 4, $R_{\infty,D}$ was 10×10^6 when the Mach number was increasing and 6×10^6 when the Mach number was decreasing. The data for the other stations in the cup and on the lip, in general, indicate some increase in $h/h_{0,th}$ for larger values of $R_{\infty,D}$.

Figure 11 shows the distribution of heat transfer over the nose surface in the form of Stanton number based on free-stream properties (eq. (6)) as a function of x/s for the 11 in-line stations at several times during the high Mach number part of the flight. The theoretical $N_{St,\infty}$ values for hemispherical-nose stagnation point obtained from reference 10, as previously noted, are also shown.

At all Mach numbers, the Stanton number was relatively constant over the center of the cup and increased to a maximum just inside the lip. On the lip $(x/s = 1)$, $N_{St,\infty}$ was somewhat less than just inside the lip. The measurement location just behind the lip $(x/s = 1.045)$ was just behind the point of tangency of the lip curvature with the cylindrical section. The Stanton number at this point was considerably less than at the lip, but not as low as at the next rearward station $(x/s = 1.16)$, where the extremely low Stanton number probably indicated separated flow. Farther rearward along the cylinder the $N_{St,\infty}$ values increased to approximately the values at the lip.

The value of $N_{St,\infty}$ in the center portion of the cup was roughly 10 percent, and that just inside the lip was roughly 70 percent, of the theoretical hemisphere stagnation-point value. There was some Mach number influence on these ratios, as was seen in figure 10.

For the sake of general interest, the experimental data on the cup nose were compared with the familiar flat-plate and conical theories (ref. 11). Using local conditions as determined from the pressure distribution of figure 9 and basing Reynolds number on length along the surface from the stagnation point, a computation of theoretical laminar and turbulent values was made. Conical theory was arbitrarily used for the locations inside and including the lip, on the basis of the three-dimensional aspects of the cup. Flat-plate theory was used for the stations along the cylindrical part of the nose. These theories are shown by the curves in figure 11. The laminar cone theory is in surprisingly good agreement with the data in the cup and on the lip. Comparison of the data on the cylinder with flat-plate theory would indicate that the boundary layer on the cylinder was transitional; at the forward cylinder stations the data are fairly close to the laminar flat-plate theory, while at the last cylinder station the data are approaching the turbulent theory except at the later times when Reynolds number is decreasing.

Angle of Attack and Symmetry of Heating

A normal and a transverse accelerometer were included in the instrumentation to determine whether the model departed from a zero angle-of-attack flight condition. Angles of attack, computed from the time histories of acceleration, model weight, dynamic pressure, and an estimated lift coefficient for the model varied between 0.05° and 0.11° at times after 5.8 seconds, when the transitory oscillation following second-stage ignition damped out.

In order to determine the symmetry of heating on the nose, thermocouples 3b, 6b, 7b, and 10b were located on the nose at positions diametrically opposite corresponding thermocouples of the 11 in-line groups. Thermocouple 7c, on the lip, was located 90° from the in-line group. Figures 12(a) and 12(b) show the location of these thermocouples.

Since lateral heat-flow computations could not be made for these measurement stations, their one-dimensional heating rates are compared with the one-dimensional rates for the corresponding in-line stations. The comparisons indicate that there were only small asymmetries in the heating in the cup and on the lip but that there was some difference in the heating on opposite sides of the cylinder at station 10, somewhat behind the lip.

General Results in Relation to Other Tests

Preflight-jet tests at a Mach number of 2 and $R_{\infty,D} = 3 \times 10^6$ on a model similar to that of the present test showed heating rates at

the stagnation point equal to 0.45 times the theoretical hemisphere stagnation-point value. (See ref. 4.) This is approximately 4.5 times the stagnation-point rates obtained in the present test. While the highest heat-transfer rates occurred just inside the lip in both tests, the magnitude was 1.23 times the theoretical hemisphere stagnation-point value in the test of reference 4, but only about 0.7 of the theoretical hemisphere stagnation-point value in the present flight test.

In reference 4 the experimental total heat input to the surface of the cup nose including the lip was compared with the computed laminar-theory total heat input to a hemispherical nose and to a flat face having the same diameter. The cup nose had 1.43 times the total heat input of the hemisphere and 2.1 times that of the flat face. A similar comparison of the present data at $M_\infty = 5$ shows 0.55 times the total heat input to the hemisphere and 0.76 times that to the flat face. The reason for the difference between the present test and that of reference 4 is not yet understood.

As a result of the very low heating rates (relative to those of ref. 4) noted in preliminary analysis of the present data, investigations of the nose shape were also undertaken in the Langley Gas Dynamics Branch and Langley Unitary Plan wind tunnel. Results of these tests, along with those from the preflight jet and the present test, are presented in figure 13 as ratios of $h/h_{o,th}$ plotted against Reynolds number based on diameter. This figure is essentially as presented in reference 6 except for the inclusion of complete data from the present test.

The tests made by the Gas Dynamics Branch and reported in reference 6 showed that unstable oscillating flow occurred aperiodically on the nose at a Mach number of 1.98 for $R_{\infty,D} \approx 3 \times 10^6$ and at a Mach number of 4.95 for $R_{\infty,D}$ values ranging from 4.4×10^6 to 11×10^6. The unstable flow, which occurred only near zero angle of attack, was accompanied by an increase in heat-transfer rate at the stagnation point of six to seven times the steady-flow values. (See fig. 13.) Furthermore, the steady-flow values at the stagnation point varied from 20 to 50 percent of the theoretical hemisphere stagnation-point values, depending on Reynolds number and Mach number. Thus, the steady-flow rates were approximately five times as great as the present flight-test results at the same Reynolds number, and the unsteady rates were approximately 30 times as great as the present flight-test results at the same Reynolds number.

Unpublished data obtained by Robert L. Stallings, Jr., and Paige B. Burbank in the Langley Unitary Plan wind tunnel indicate that the unsteady oscillatory flow, accompanied by high heat-transfer rates, can occur at an angle of attack of 7.5° at a Mach number of 2.5 and $R_{\infty,D} = 2.16 \times 10^6$,

and at an angle of attack of 15° at a Mach number of 4.5 and $R_{\infty,D} = 1.02 \times 10^6$. These tests also indicated that the steady-flow heat rates at the stagnation point and just inside the lip were 0.18 and 0.89 times the hemisphere stagnation-point values, respectively, for a Mach number of 2.5 and $R_{\infty,D} = 1.02 \times 10^6$. Some stagnation-point values from these tests are shown in figure 13.

The stable type of heating data of references 4 and 6 and the unpublished data of the Langley Unitary Plan wind tunnel are not inconsistent with each other when correlated on the basis of $R_{\infty,D}$. This is apparent from figure 13 and was previously shown in reference 6. It may be noted that the effect of $R_{\infty,D}$ on stagnation-point heat rates was negligible in the present test for the $R_{\infty,D}$ range from 6×10^6 to 10×10^6 at a Mach number of 4.

The reason for the differences between these tunnel data and the data of the present flight test is as yet unknown.

CONCLUSIONS

The aerodynamic heat transfer to a concave hemispherical nose has been measured in free flight at Mach numbers from 3.5 to 6.6 with corresponding Reynolds numbers based on nose diameter from 7.4×10^6 to 14×10^6. The results of the investigation were as follows:

1. The heat-transfer coefficients at the center point of the nose varied from 0.05 to 0.13 times the theoretical hemisphere stagnation-point values at Mach numbers from 4 to 6.6, respectively, and were approximately 1/5 as great as steady-flow tunnel results.

2. At other locations within 40° of the center point of the nose, the heat-transfer coefficients were approximately 0.1 of the theoretical hemisphere stagnation-point values.

3. The heat-transfer coefficients were greater at locations near the lip, and the highest values, which occurred just inside the lip, were from 0.6 to 0.8 of the theoretical hemisphere stagnation-point values.

4. At a Mach number of 5 the total heat input, integrated over the surface of the cup nose, was 0.55 times the theoretical value for a hemisphere nose with a laminar boundary layer and 0.76 times the theoretical value for a flat face.

5. Extremely high heating rates at the center point (on the order of 30 times the stagnation point values of the present test), which have occurred in conjunction with unsteady oscillatory flow around cup noses in wind-tunnel tests at Mach and Reynolds numbers within the present test range, were not observed.


Langley Research Center,
    National Aeronautics and Space Administration,
        Langley Field, Va., September 9, 1958.

REFERENCES

1. Garland, Benjamine J., Swanson, Andrew G., and Speegle, Katherine C.: Aerodynamic Heating and Boundary-Layer Transition on a 1/10-Power Nose Shape in Free Flight at Mach Numbers up to 6.7 and Free-Stream Reynolds Numbers up to 16×10^6. NACA RM L57E14a, 1957.

2. Stoney, William E., Jr., and Swanson, Andrew G.: Heat Transfer Measured on a Flat-Face Cylinder in Free Flight at Mach Numbers up to 13.9. NACA RM L57E13, 1957.

3. Carter, Howard S., and Bressette, Walter E.: Heat Transfer and Pressure Distribution on Six Blunt Noses at a Mach Number of 2. NACA RM L57C18, 1957.

4. Markley, J. Thomas: Heat Transfer and Pressure Measurement on a 5-Inch Hemispherical Concave Nose at a Mach Number of 2.0. NACA RM L58C14a, 1958.

5. Hopko, Russell N., and Strass, H. Kurt: Some Experimental Heating Data on Convex and Concave Hemispherical Nose Shapes and Hemispherical Depressions on a 30° Blunted Nose Cone. NACA RM L58A17a, 1958.

6. Cooper, Morton, Beckwith, Ivan E., Jones, Jim J., and Gallagher, James J.: Heat-Transfer Measurements on a Concave Hemispherical Nose Shape With Unsteady-Flow Effects at Mach Numbers of 1.98 and 4.95. NACA RM L58D25a, 1958.

7. Stoney, William E., Jr.: Aerodynamic Heating of Blunt Nose Shapes at Mach Numbers up to 14. NACA RM L58E05a, 1958.

8. Hill, P. R.: A Method of Computing the Transient Temperature of Thick Walls From Arbitrary Variation of Adiabatic-Wall Temperature and Heat-Transfer Coefficient. NACA TN 4105, 1957.

9. O'Sullivan, William J., Jr.: Some Thermal and Mechanical Properties of Inconel at High Temperatures for Use in Aerodynamic Heating Research. Proc. A.S.T.M., vol. 55, 1955, pp. 757-763.

10. Fay, J. A., and Riddell, F. R.: Theory of Stagnation Point Heat Transfer in Dissociated Air. Jour. Aero. Sci., vol. 25, no. 2, Feb. 1958, pp. 73-85, 121.

11. Van Driest, E. R.: The Problem of Aerodynamic Heating. Aero. Eng. Rev., vol. 15, no. 10, Oct. 1956, pp. 26-41.

TABLE I.- INSIDE WALL TEMPERATURES FROM FAIRED CURVES

Time, sec	Temperature, °F, at thermocouple number -															
	1	2	3a	3b	4	5	6a	6b	7a	7b	7c	8	9	10a	10b	11
2.0	66	74	73	70	80	74	76	79	74	74	70	69	75	69	77	73
2.2	66	74	74	70	81	75	79	82	74	75	73	70	75	70	78	75
2.4	66	75	75	72	81	76	80	86	75	76	76	70	75	72	79	76
2.6	66	75	75	74	82	78	86	94	77	81	80	71	76	75	80	81
2.8	66	75	75	75	84	83	96	105	81	89	86	73	76	80	85	92
3.0	67	76	76	76	90	89	110	118	90	99	94	74	76	89	95	106
3.2	68	77	80	80	97	98	127	135	99	112	105	75	77	102	108	124
3.4	70	78	85	83	102	110	144	155	110	129	117	76	78	115	120	143
3.6	74	80	90	86	108	119	160	174	125	143	129	77	79	129	133	160
3.8	76	83	94	89	113	128	177	191	139	156	139	80	80	140	145	177
4.0	79	85	99	92	118	136	192	208	151	170	148	82	80	150	155	192
4.2	82	87	103	95	122	145	206	225	164	182	156	87	81	160	165	205
4.4	85	89	107	98	127	151	220	237	176	195	165	95	81	169	174	219
4.6	87	91	111	100	131	158	232	248	187	208	172	101	82	177	182	230
4.8	90	94	115	102	136	165	244	257	199	220	180	107	83	185	187	241
5.0	92	95	119	106	140	176	255	262	210	229	187	110	84	191	194	250
5.2	95	100	124	111	146	188	269	276	221	238	201	113	86	204	204	265
5.4	96	107	128	120	158	205	292	306	239	256	226	115	89	224	220	290
5.6	103	119	141	134	176	229	328	359	267	289	265	119	92	250	240	330
5.8	116	134	162	154	205	267	383	429	320	341	325	125	96	283	265	386
6.0	139	157	191	181	245	322	470	524	402	414	415	140	103	322	292	465
6.2	171	190	231	215	295	399	600	652	425	515	547	166	116	367	323	567
6.4	211	232	278	256	358	498	760	833	675	645	712	200	135	420	356	704
6.6	258	280	331	300	425	609	935	1037	833	785	878	243	161	476	391	856
6.8	310	325	377	346	488	713	1087	1180	985	918	1027	297	186	538	430	982
7.0	355	360	418	390	543	796	1210	1263	1085	1017	1133	360	203	604	475	1075
7.2	386	387	452	429	590	861	1293	1304	1146	1089	1209	418	215	661	526	1150
7.4	411	410	479	460	626	910	1350	1326	1185	1135	1255	472	223	710	579	1201
7.6	430	427	500	484	654	946	1389	1336	1208	1158	1278	518	230	750	620	1237
7.8	446	441	516	501	676	975	1413	1338	1221	1170	1289	560	235	782	650	1260
8.0	457	452	530	516	695	997	1427	1333	1227	1172	1291	598	240	807	671	1275
8.2	466	461	543	528	710	1016	1431	1321	1227	1167	1285	632	245	827	687	1284
8.4	473	469	555	538	722	1030	1428	1306	1223	1160	1275	661	250	843	699	1289
8.6	477	475	564	546	732	1041	1420	1289	1215	1149	1261	685	254	855	708	1291
8.8	481	480	572	553	741	1050	1410	1271	1205	1135	1245	706	260	863	714	1291
9.0	484	484	578	559	750	1055	1398	1253	1192	1121	1230	724	265	869	720	1290
9.2	487	487	583	564	756	1060	1382	1235	1176	1106	1213	738	270	874	723	1286
9.4	489	490	587	568	762	1062	1366	1218	1163	1090	1196	750	275	876	726	1281
9.6	490	492	591	572	768	1063	1347	1200	1149	1074	1179	759	280	878	726	1276
9.8	490	494	594	575	773	1064	1330	1184	1135	1058	1162	766	285	879	727	1270
10.0	491	495	596	579	777	1064	1313	1166	1121	1041	1145	771	290	880	728	1264
10.2	490	498	598	580	780	1061	1297	1149	1107	1023	1128	775	295	880	729	1255
10.4	490	500	600	581	781	1059	1281	1131	1094	1007	1112	777	300	879	729	1248
10.6	490	500	601	583	783	1056	1265	1115	1080	991	1096	780	305	878	729	1240
10.8	490	502	602	585	784	1054	1249	1099	1066	976	1080	781	310	876	729	1232
11.0	489	504	603	585	784	1050	1234	1084	1052	963	1065	784	315	875	729	1224
11.2	489	505	604	585	784	1046	1218	1070	1040	950	1050	785	320	874	729	1215
11.4	488	506	604	585	785	1043	1203	1056	1026	937	1035	785	325	873	728	1207
11.6	488	507	605	585	785	1040	1187	1041	1014	926	1020	785	330	871	728	1198
11.8	488	509	605	586	784	1035	1172	1028	1001	915	1005	785	335	870	727	1190
12.0	488	510	605	586	783	1031	1157	1014	989	904	991	785	340	869	726	1180
12.2	487	510	605	586	782	1027	1142	1000	977	892	978	785	345	867	726	1172
12.4	487	511	606	585	781	1023	1127	987	966	881	967	783	350	866	725	1163
12.6	487	511	606	585	780	1020	1114	975	955	870	956	781	355	865	725	1155
12.8	487	510	606	585	780	1015	1101	962	945	861	946	780	360	864	725	1145
13.0	486	510	606	585	779	1011	1088	951	936	852	936	779	365	863	725	1138
13.2	486	510	606	584	777	1006	1076	940	926	844	926	776	370	862	725	1129
13.4	486	510	606	584	776	1003	1064	929	917	835	916	775	375	861	724	1120
13.6	486	510	606	583	775	999	1053	918	908	827	907	772	380	860	723	1111
13.8	486	510	606	583	774	995	1041	907	900	820	897	768	384	859	722	1102
14.0	486	510	606	582	774	990	1030	896	891	812	888	765	389	858	722	1095
14.2	486	509	606	582	772	986	1018	886	883	805	879	762	394	856	722	1086
14.4	486	509	606	582	771	981	1015	878	875	747	871	759	398	855	721	1079
14.6	486	509	606	582	770	977	994	869	868	740	863	755	402	853	721	1072
14.8	486	509	606	582	769	973	984	860	861	738	855	751	406	850	720	1067
15.0	486	509	606	581	769	969	974	851	854	726	846	749	411	849	720	1062
15.2	485	509	606	581	768	964	965	844	846	719	839	745	415	847	720	1057
15.4	485	509	605.5	580	766	960	958	835	839	712	831	742	420	846	720	1052
15.6	485	509	605.5	580	766	955	950	827	833	706	824	739	424	845	719	1047
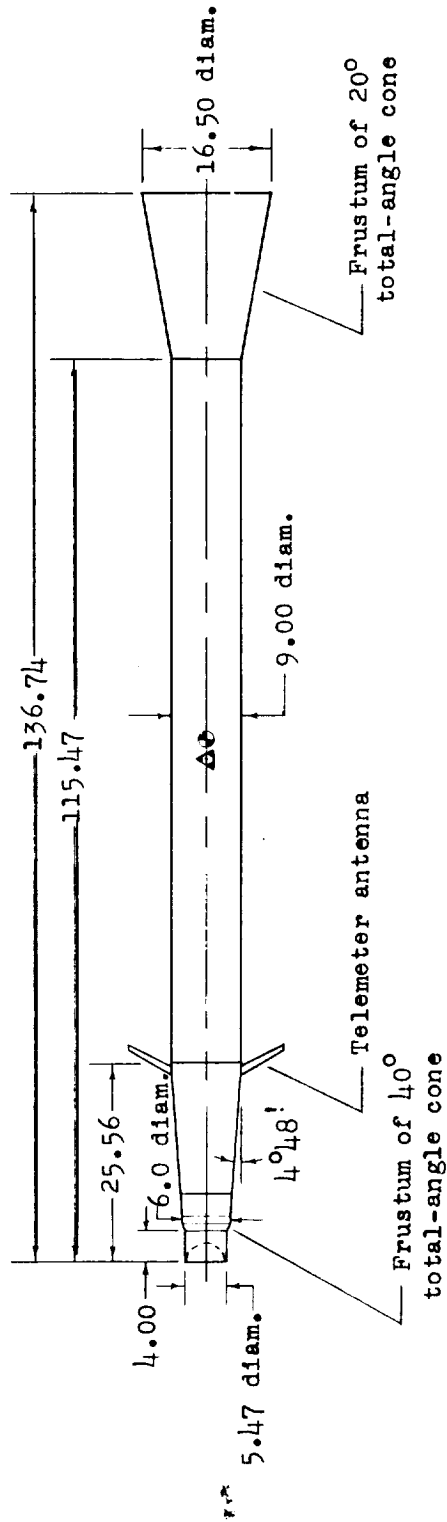
(a) General configuration. All dimensions are in inches.
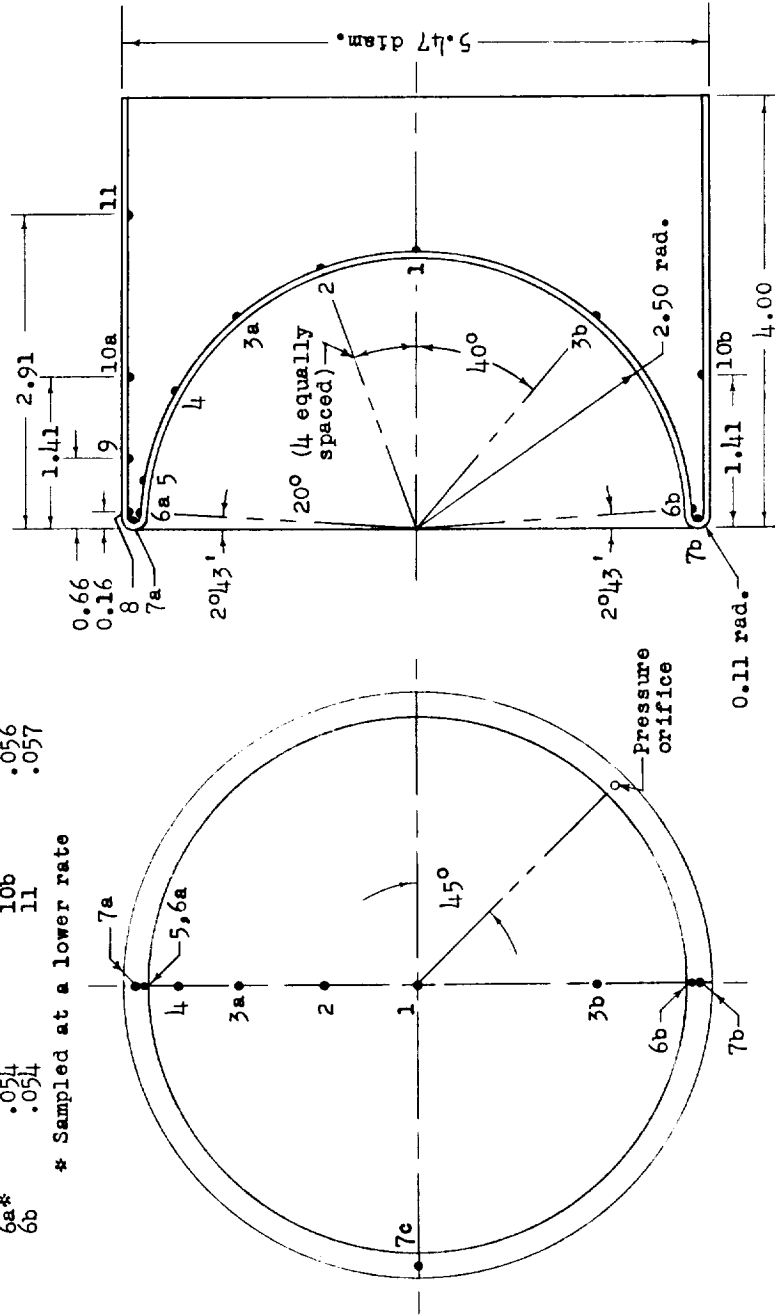
Figure 1.- Test model.
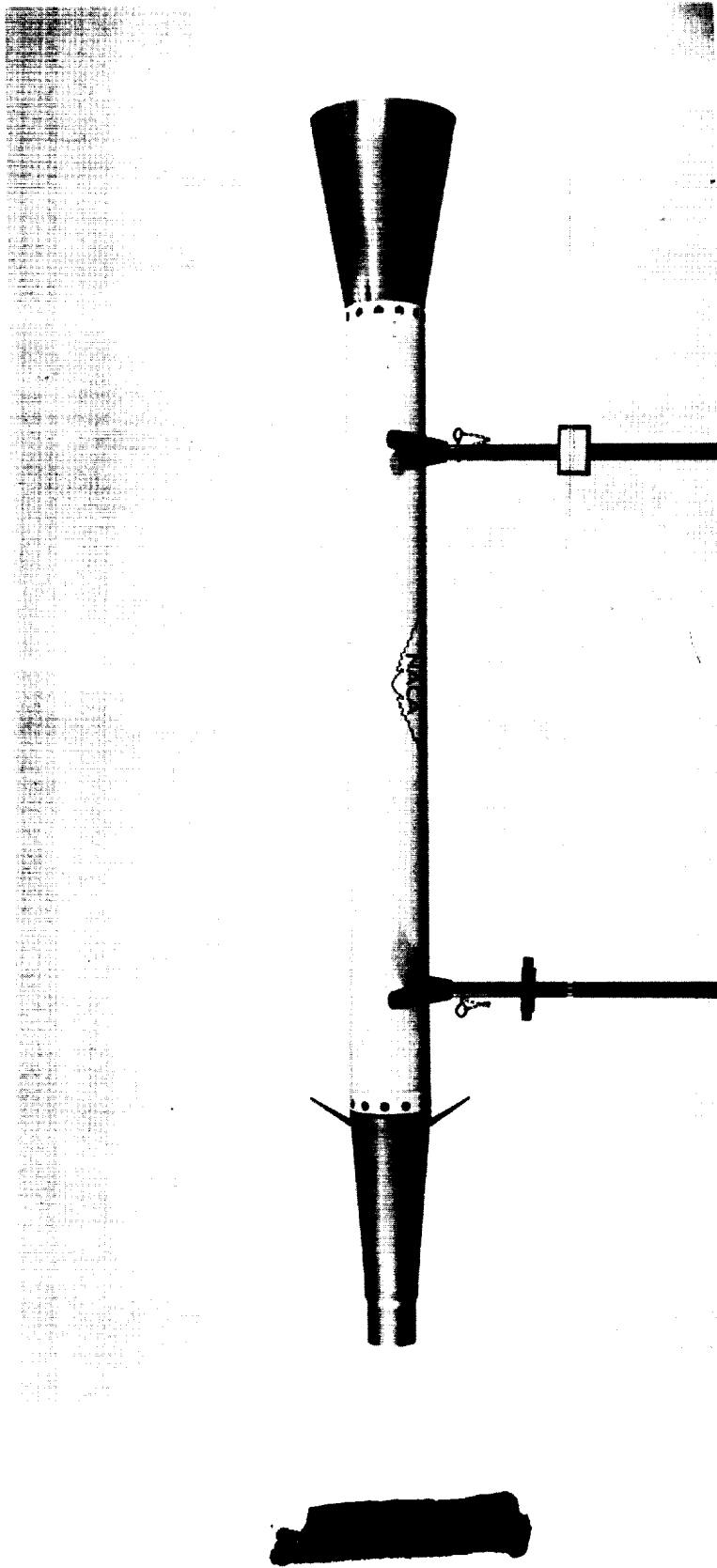
L-57-3902

(b) Photograph of the model.
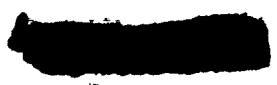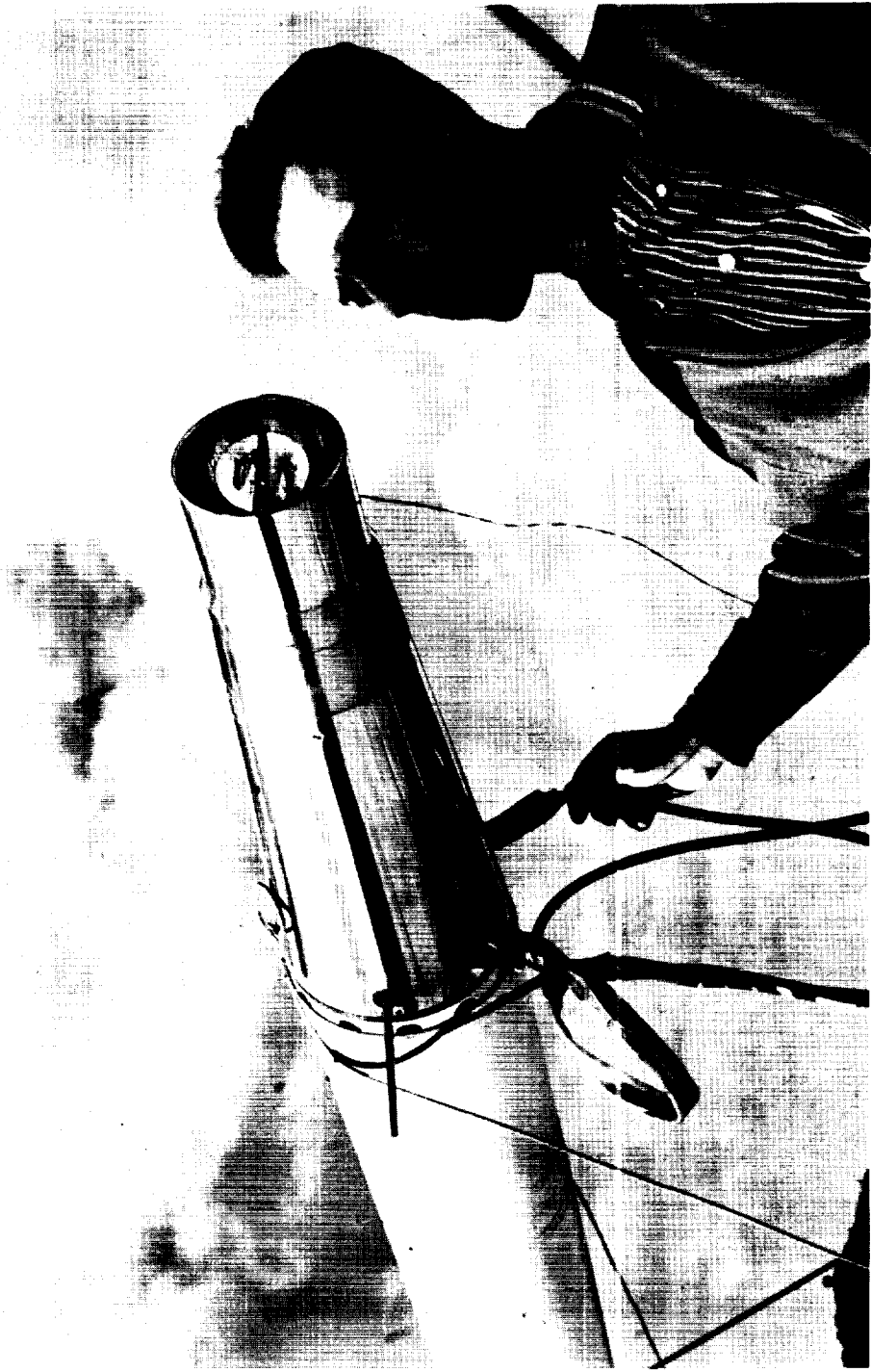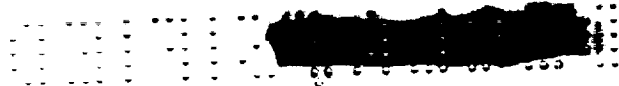
Figure 1.- Concluded.

WALL THICKNESSES

Thermocouple number	Thickness, inches	Thermocouple number	Thickness, inches
1*	.045	7a*	.062
2	.043	7b	.062
3a*	.043	7c	.064
3b	.043	8*	.060
4*	.048	9*	.048
5*	.051	10a	.057
6a*	.054	10b	.056
6b	.054	11	.057

* Sampled at a lower rate

(a) Nose detail. All dimensions are in inches.

Figure 2.- Hemispherical concave nose.

(b) Photograph of the test nose.

L-57-4337

Figure 2.- Concluded.
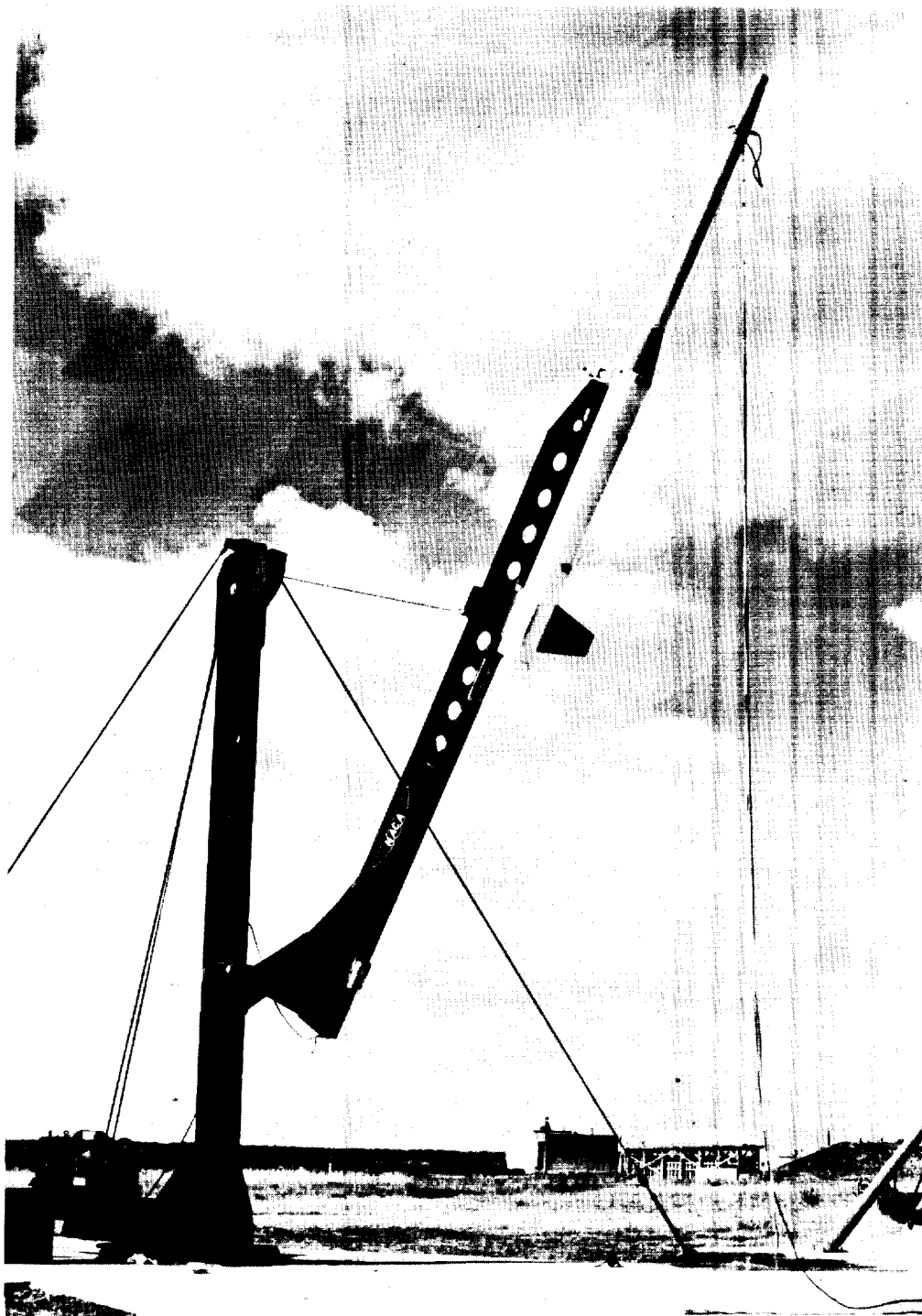
Figure 3.- Photograph of model and booster on the launcher. L-57-4336
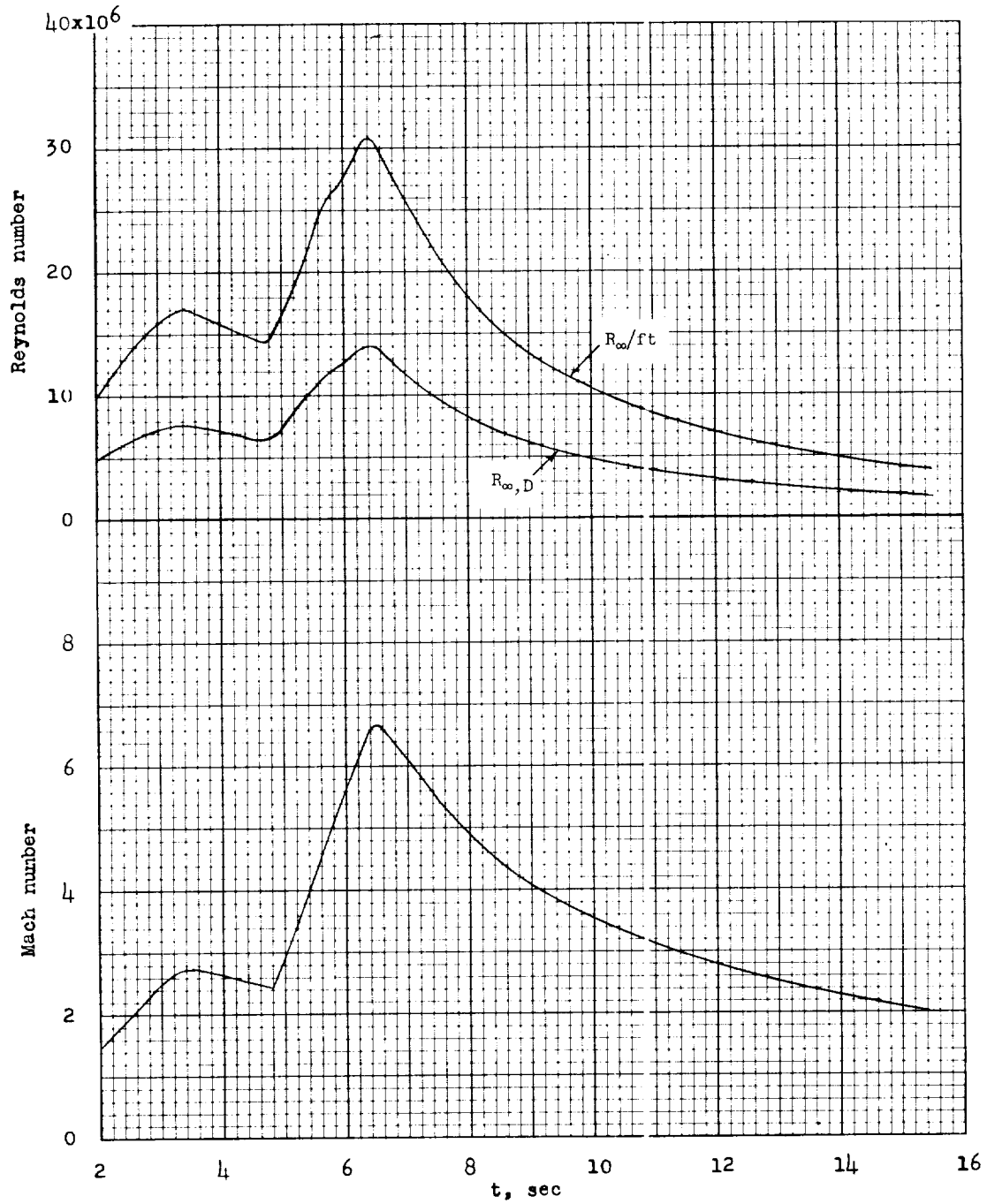
(a) Reynolds number and Mach number.

Figure 4.- Time histories of free-stream test conditions.
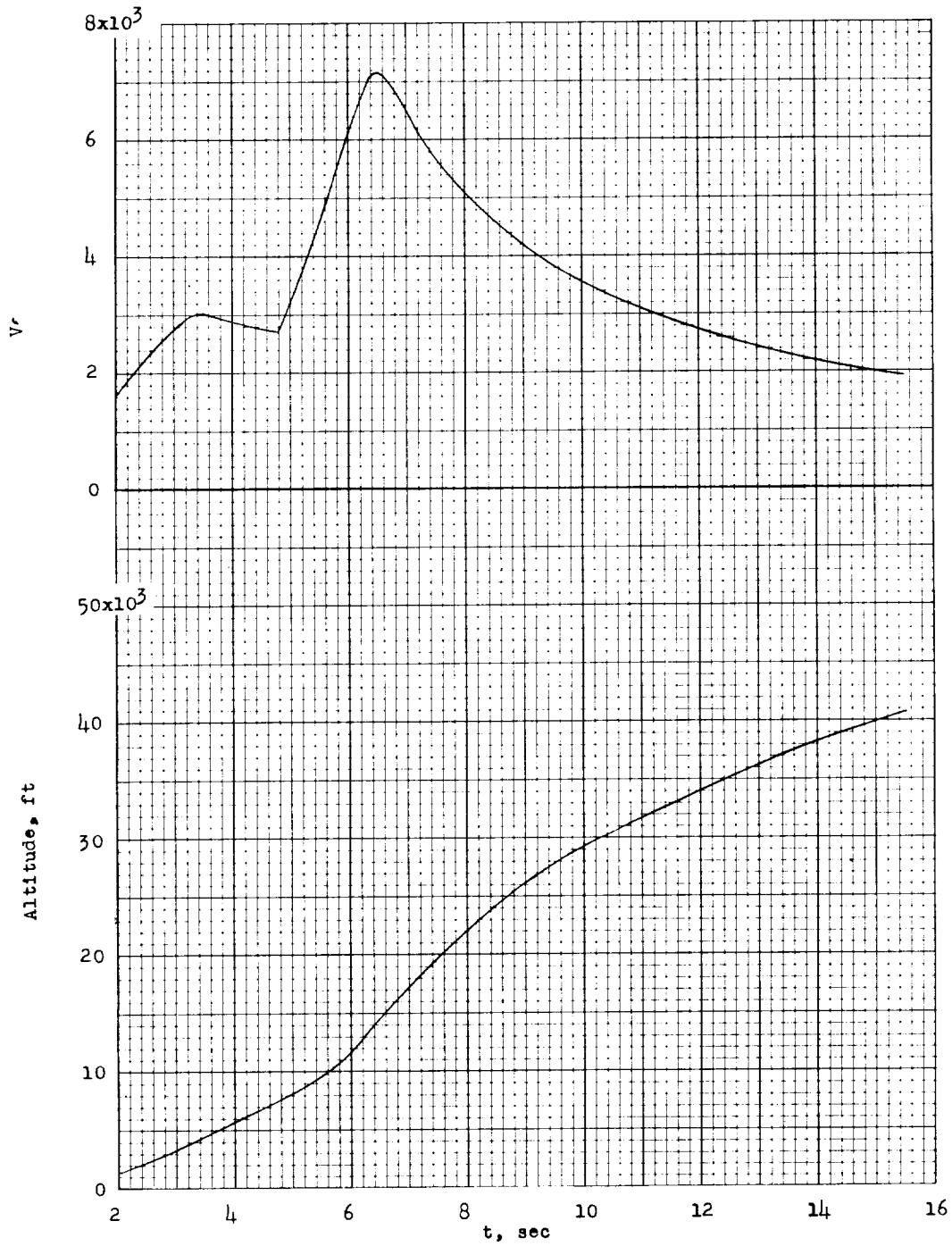
(b) Velocity and altitude.

Figure 4.- Continued.
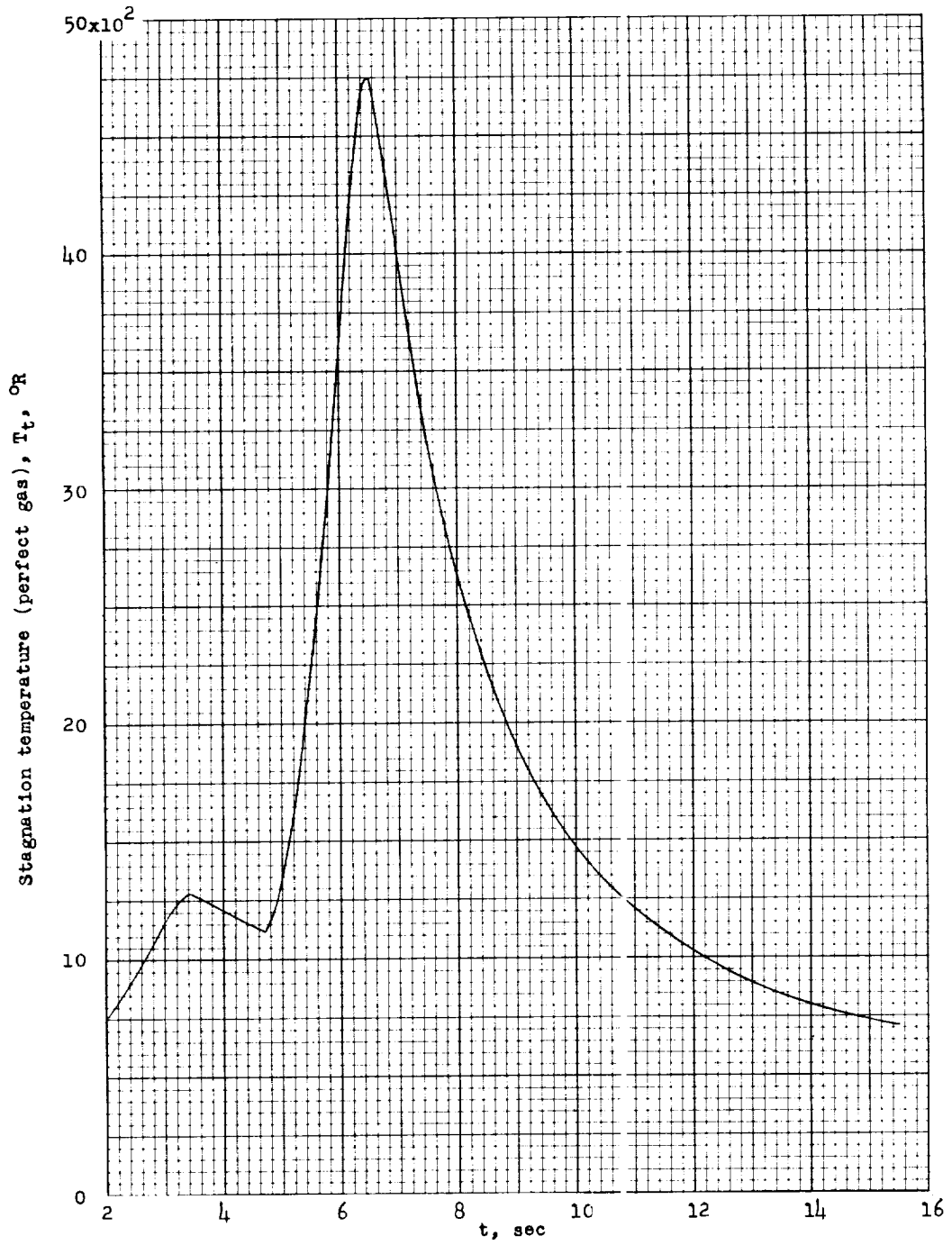
(c) Stagnation temperature.

Figure 4.- Concluded.
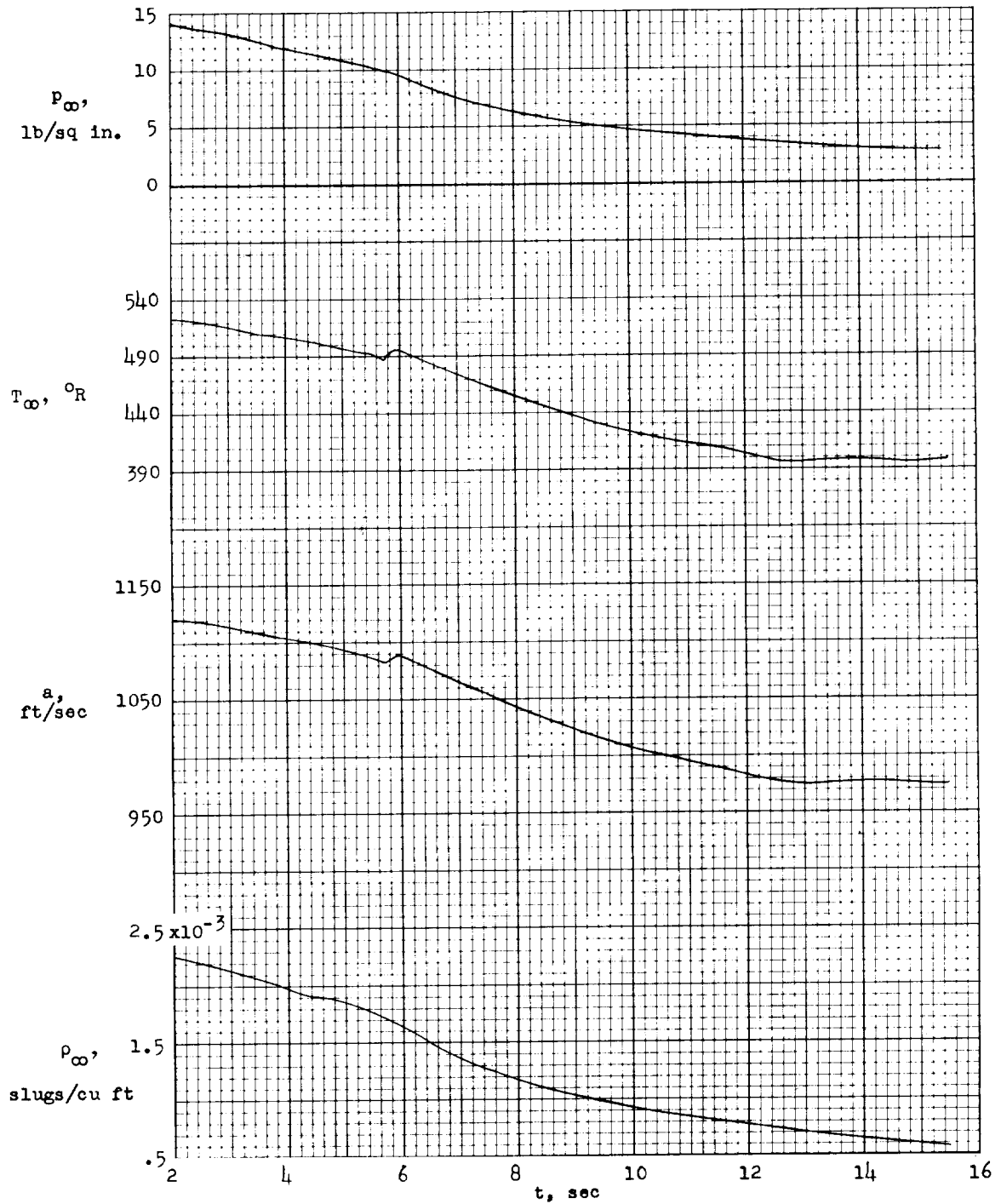
Figure 5.- Time histories of free-stream pressure, temperature, velocity of sound, and density.
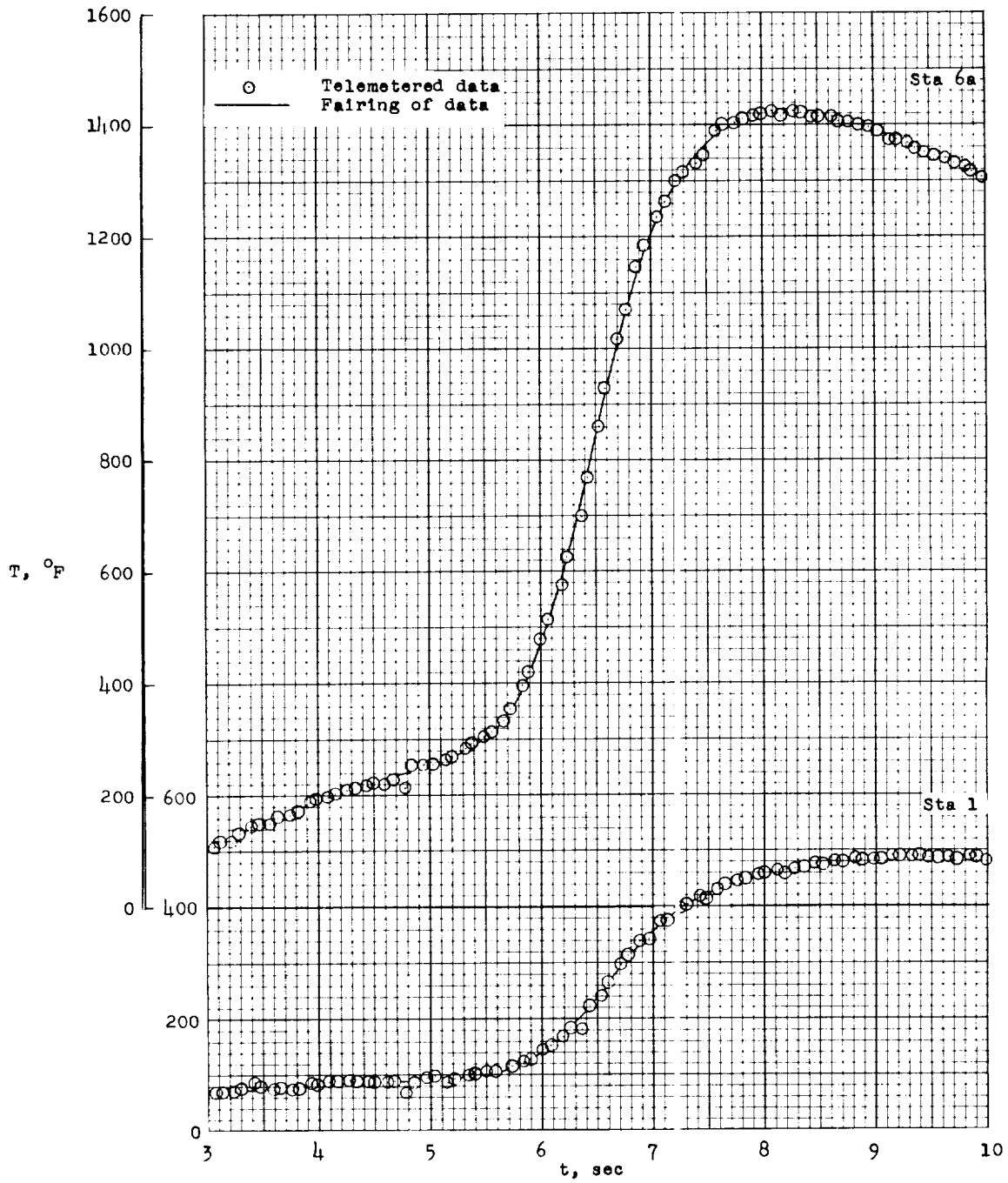
(a) Measured inside wall temperatures at stations 1 and 6a.

Figure 6.- Typical skin temperatures.
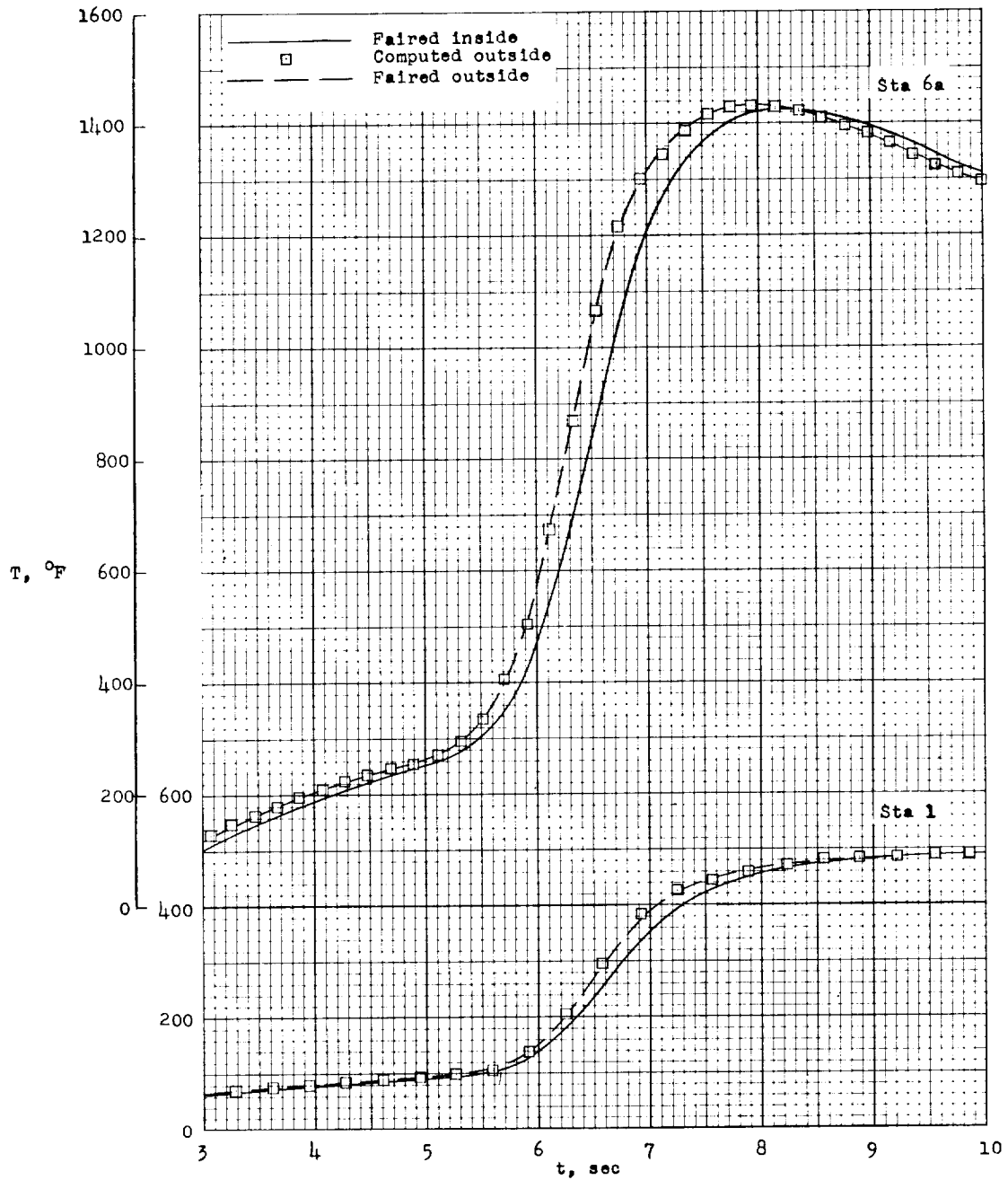
(b) Outside wall temperatures computed from faired inside wall temperatures for stations 1 and 6a.

Figure 6.- Concluded.
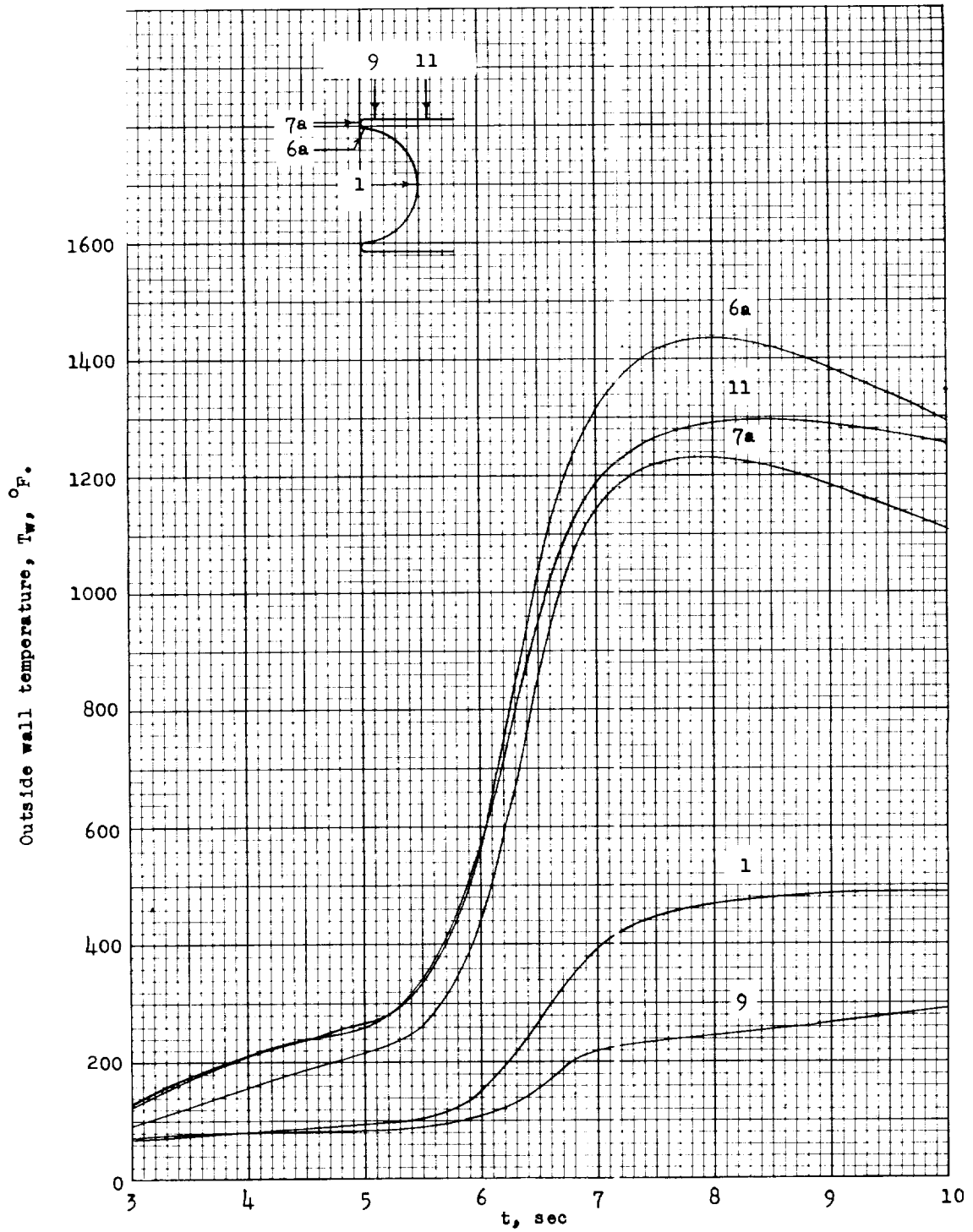
Figure 7.- Temperature distribution over the nose with time.
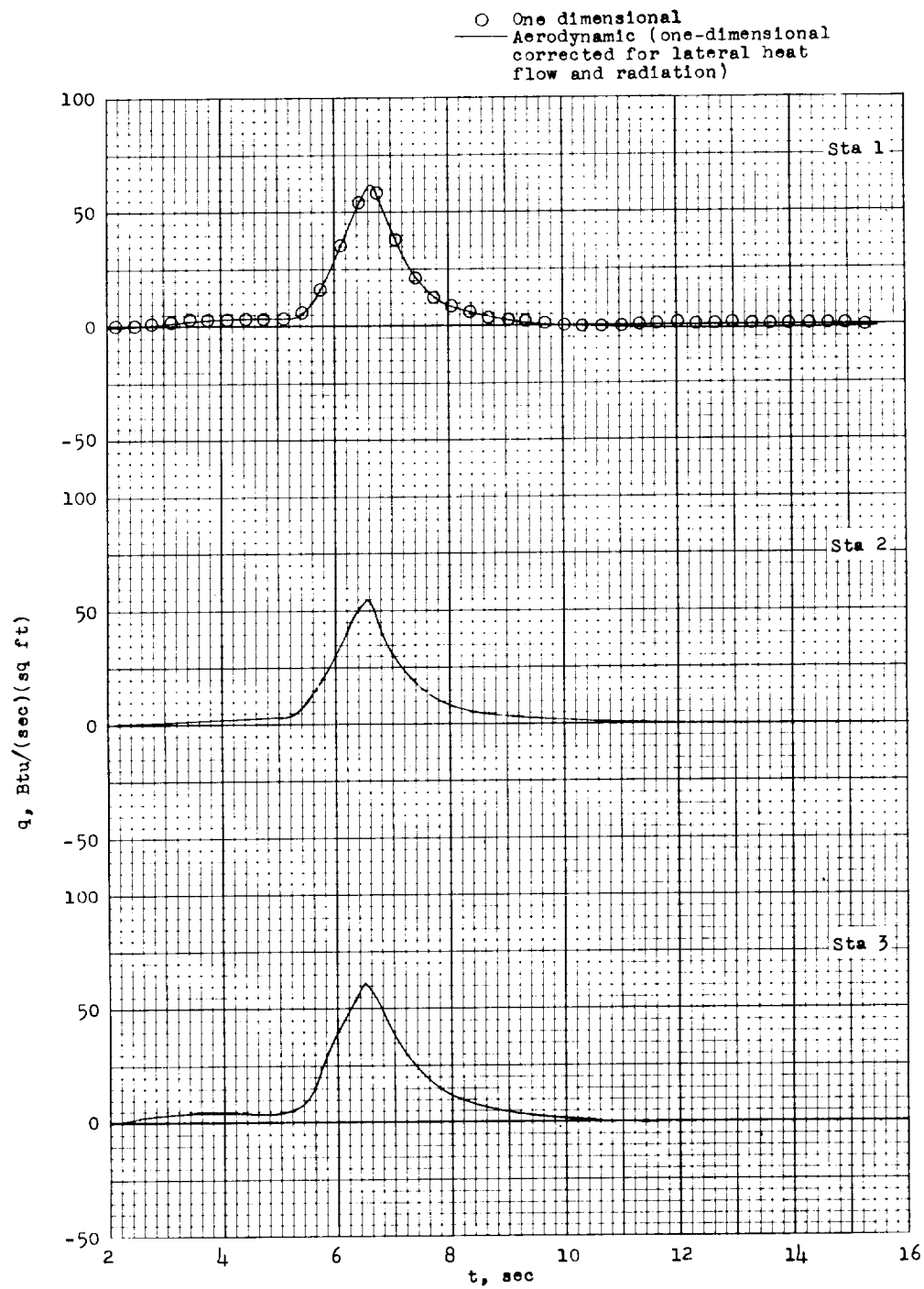
(a) Stations 1, 2, and 3 inside cup.

Figure 8.- Variation of experimental aerodynamic heating rate with time.
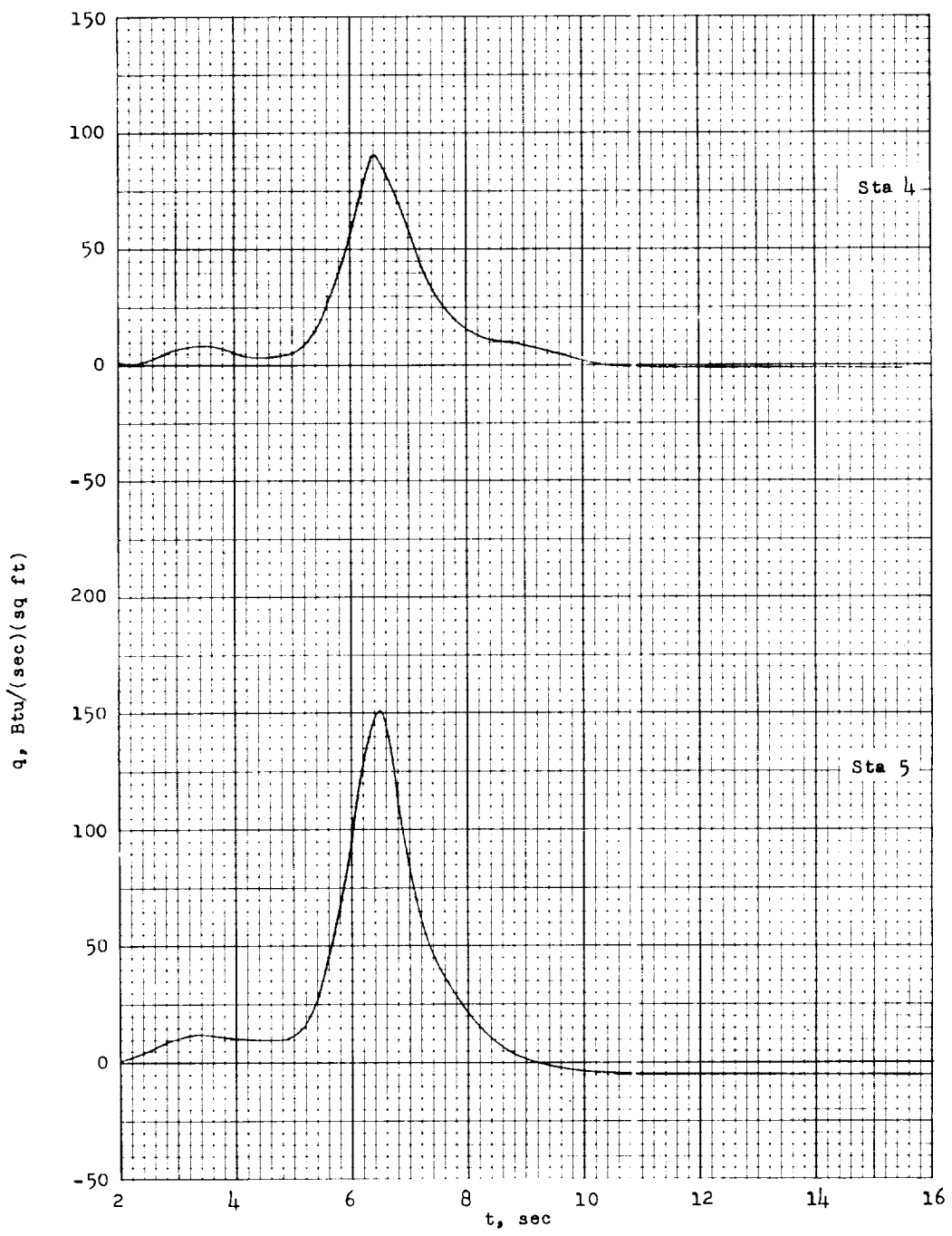
(b) Stations 4 and 5 inside cup.

Figure 8.- Continued.
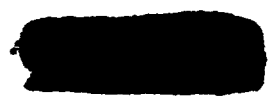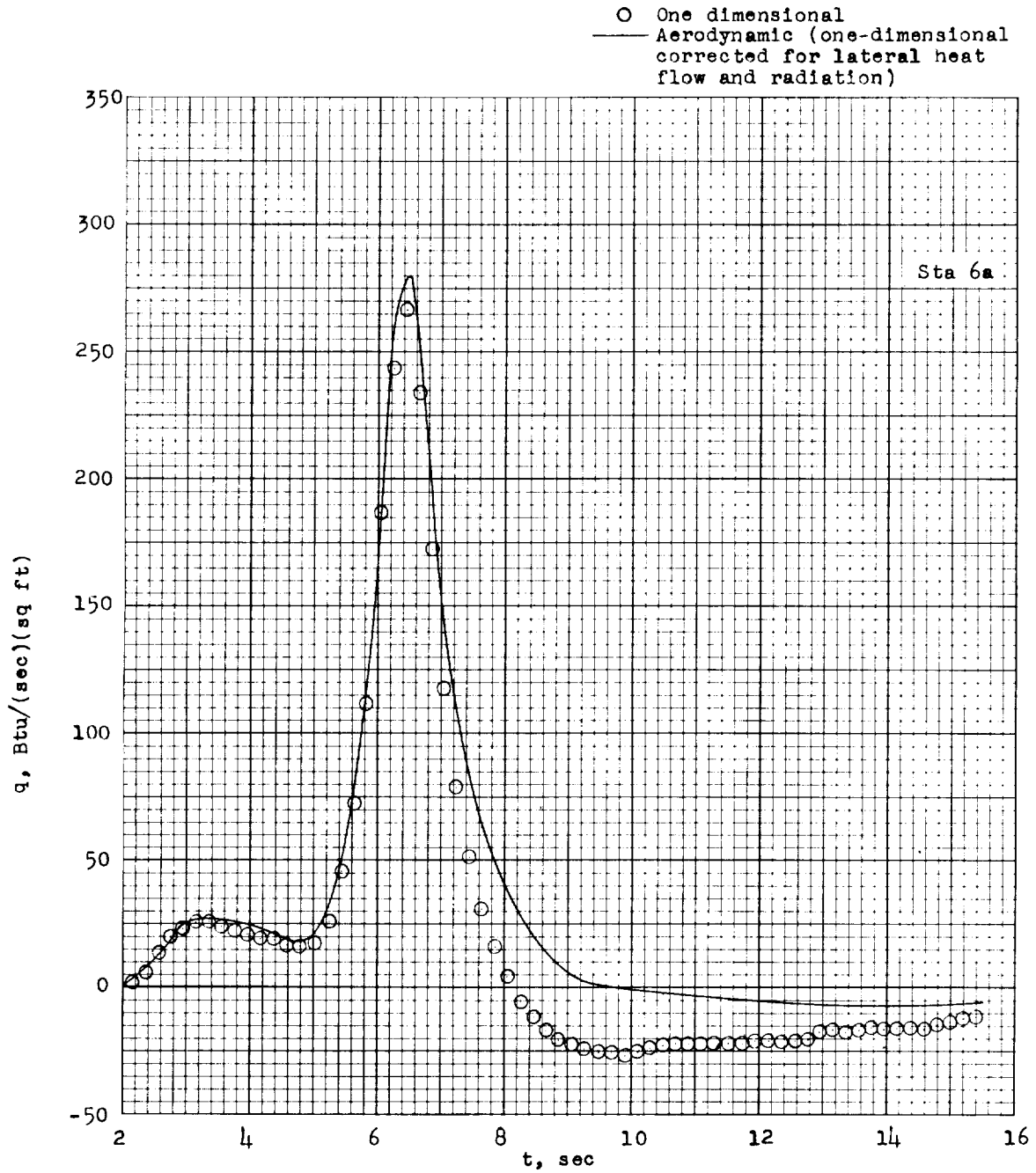
(c) Station 6a inside cup.

Figure 8.- Continued.
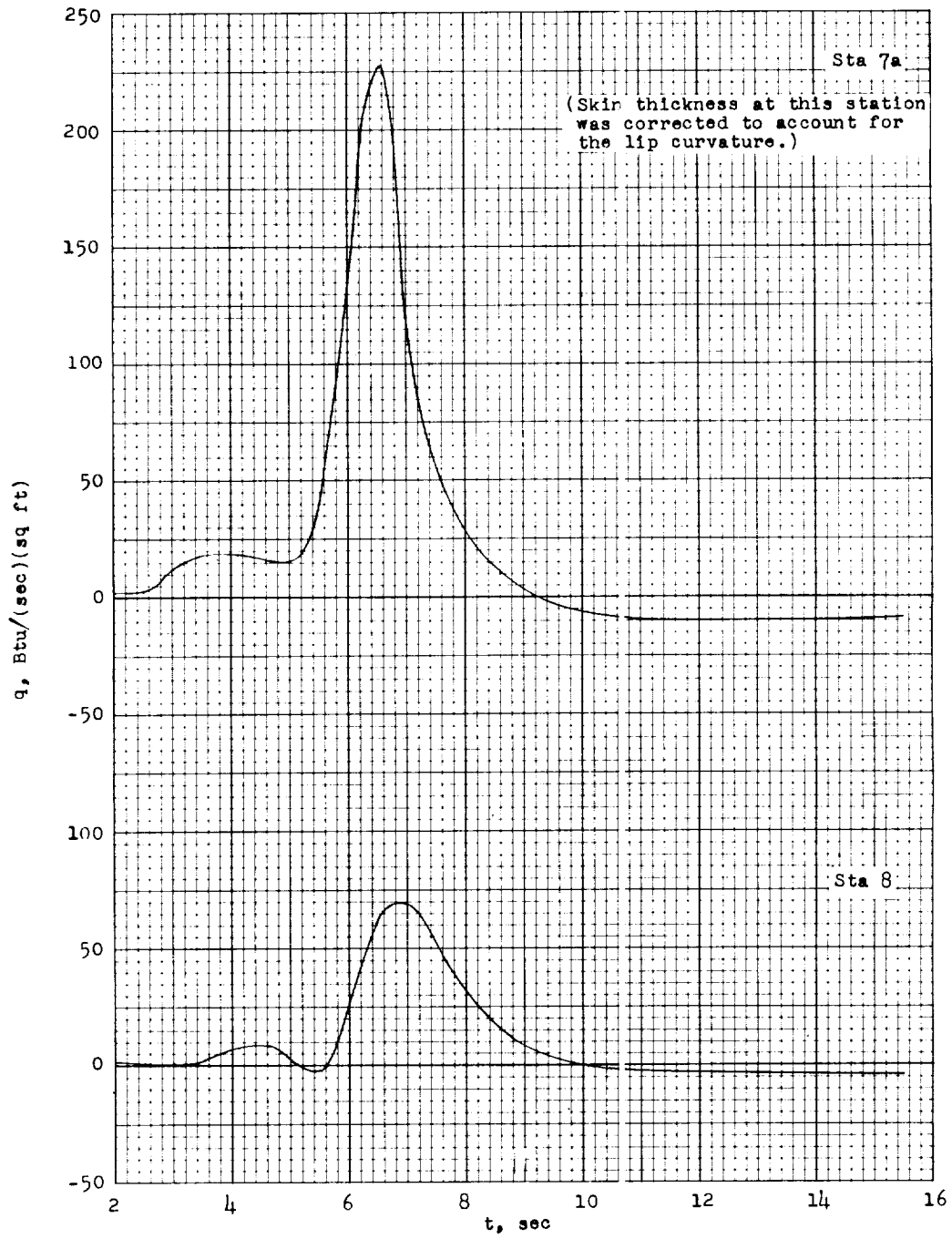
(d) Station 7a on the lip and station 8 on the cylinder.

Figure 8.- Continued.
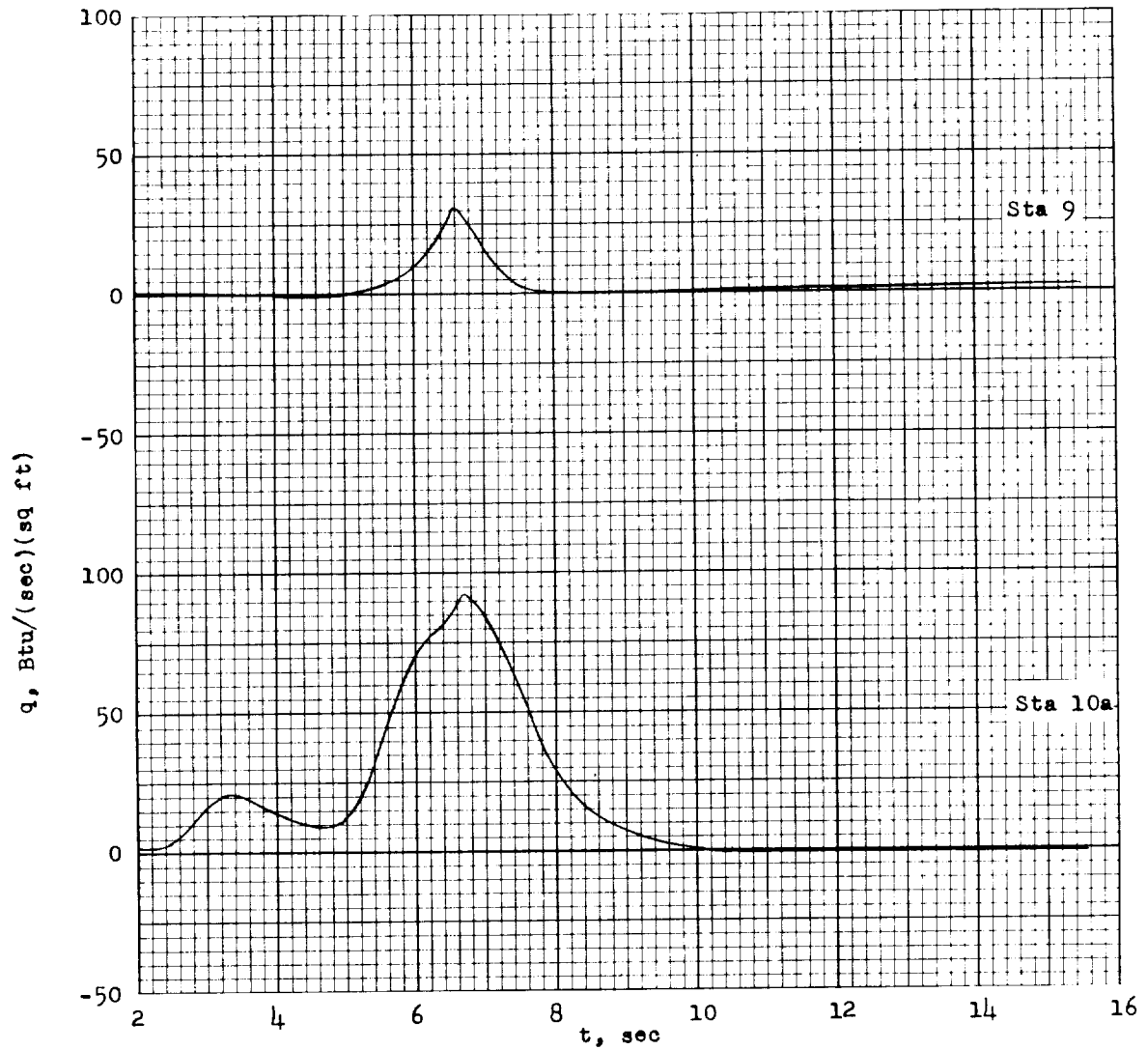
(e) Stations 9 and 10a on the cylinder.

Figure 8.- Continued.
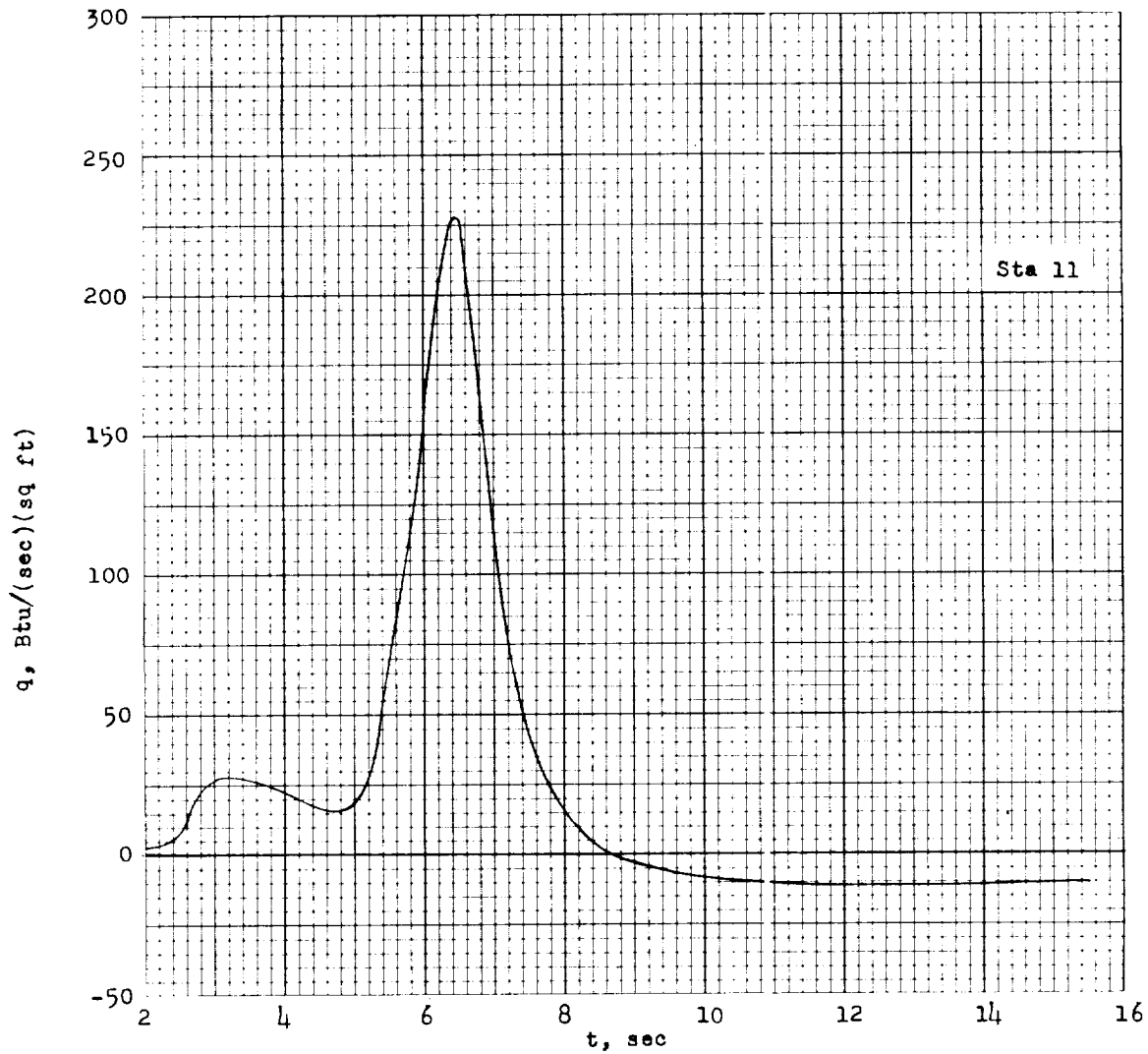
(f) Station 11 on the cylinder.

Figure 8.- Concluded.
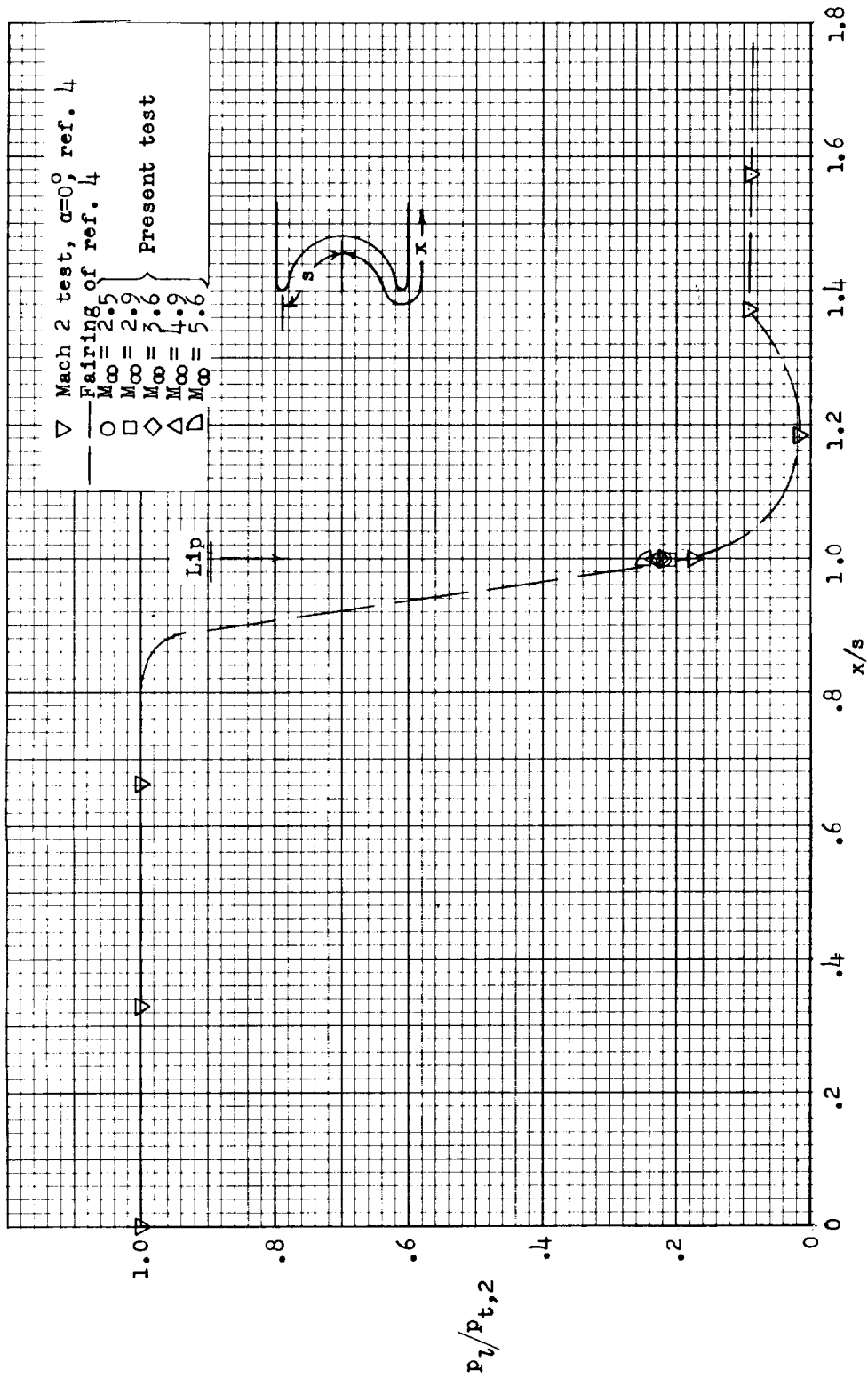
Figure 9.- Pressure distribution for a cylinder with a hemispherical concave face.
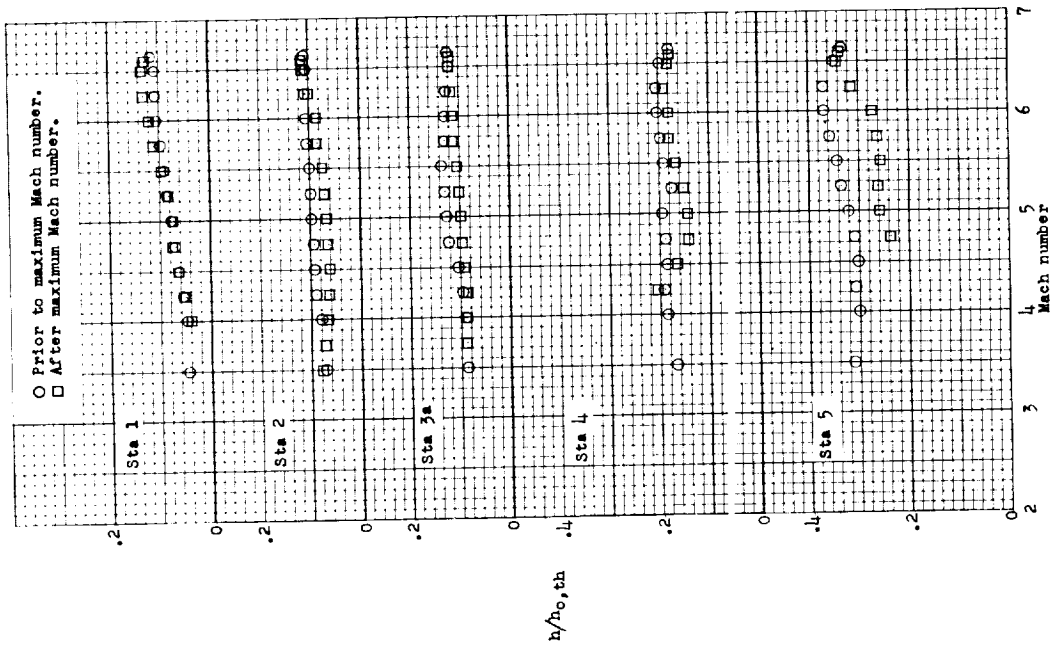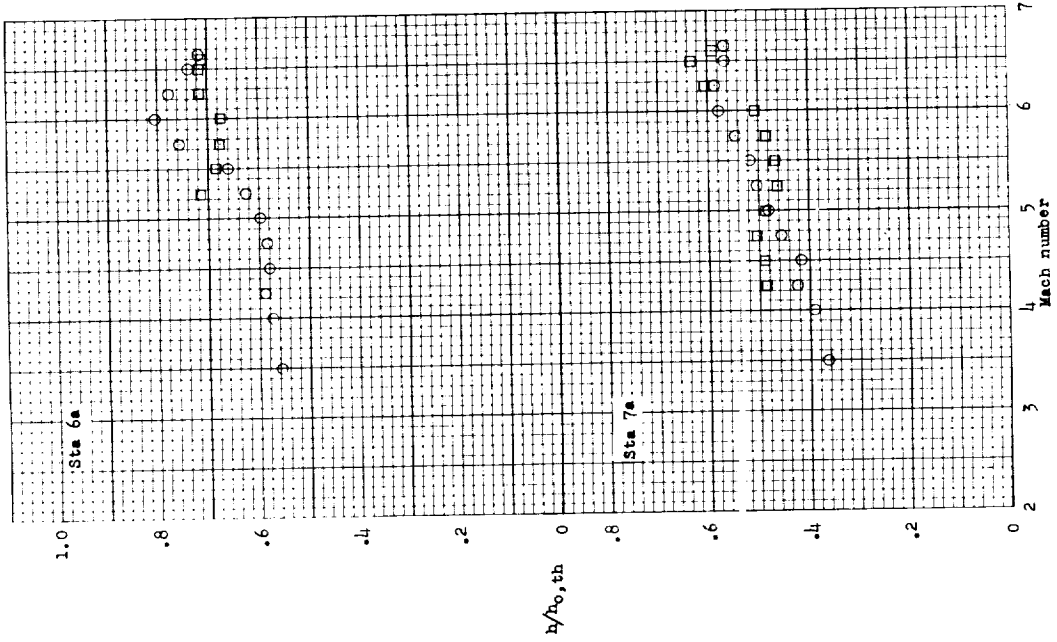
Figure 10.- Comparison of experimental heat-transfer coefficients inside the cup and on the lip in terms of theoretical hemispherical stagnation-point heating.
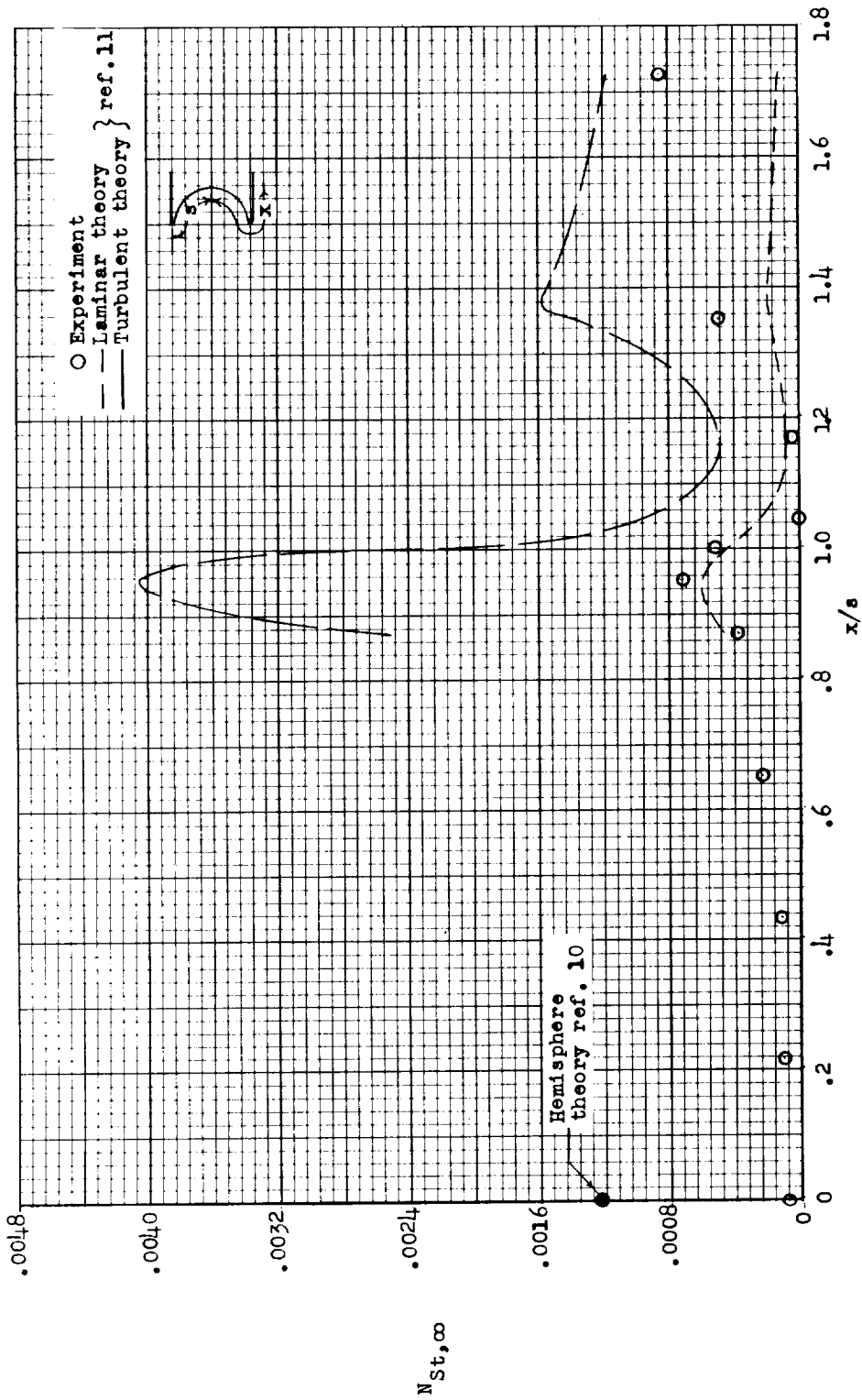
(a) $M_\infty = 4.25$; $t = 5.51$; $R_{\infty,D} = 10.5 \times 10^6$.

Figure 11.- Distribution of free-stream Stanton number along the surface of the nose.
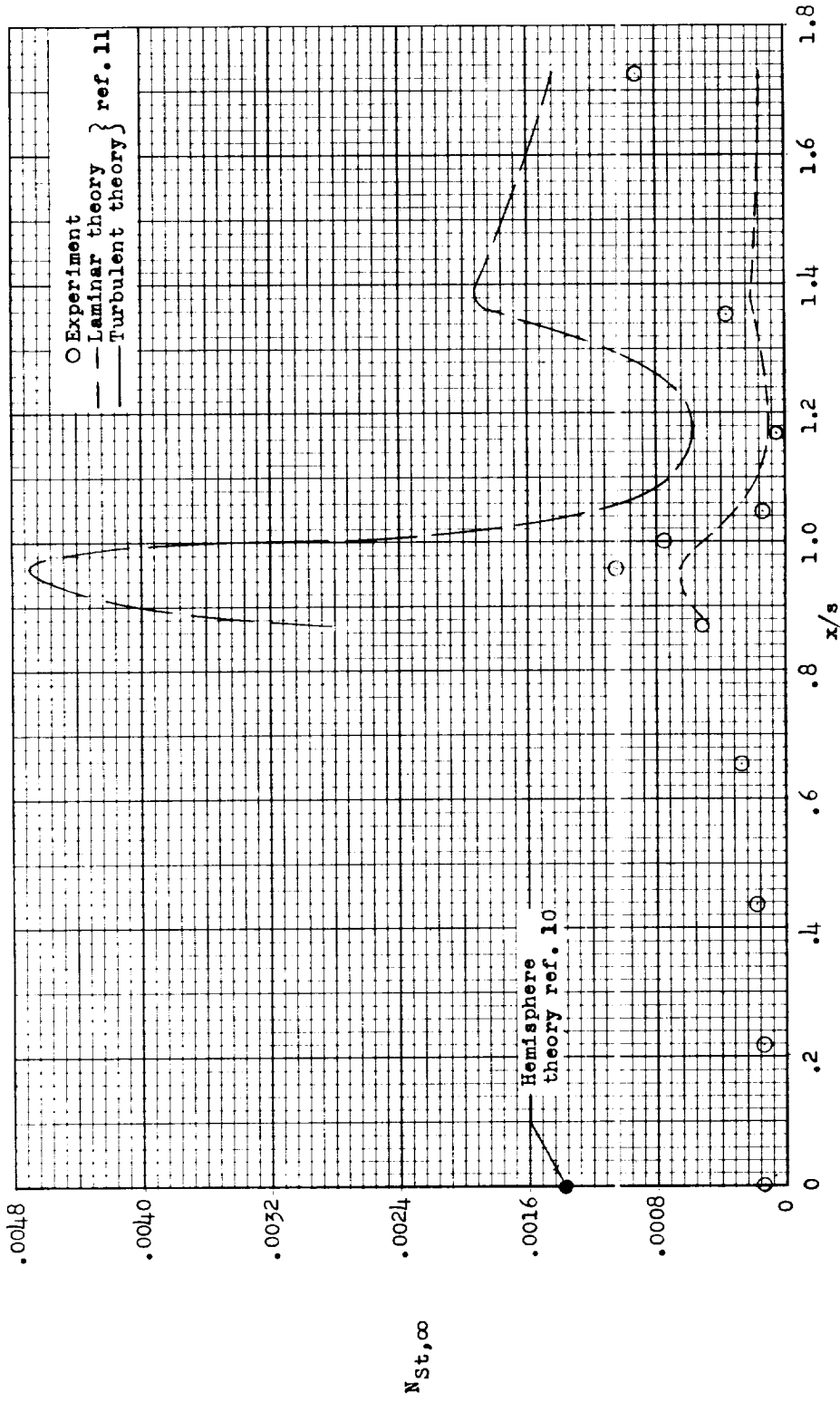
(b) $M_\infty = 5.75$; $t = 6.05$; $R_{\infty,D} = 12.9 \times 10^6$.

Figure 11.- Continued.
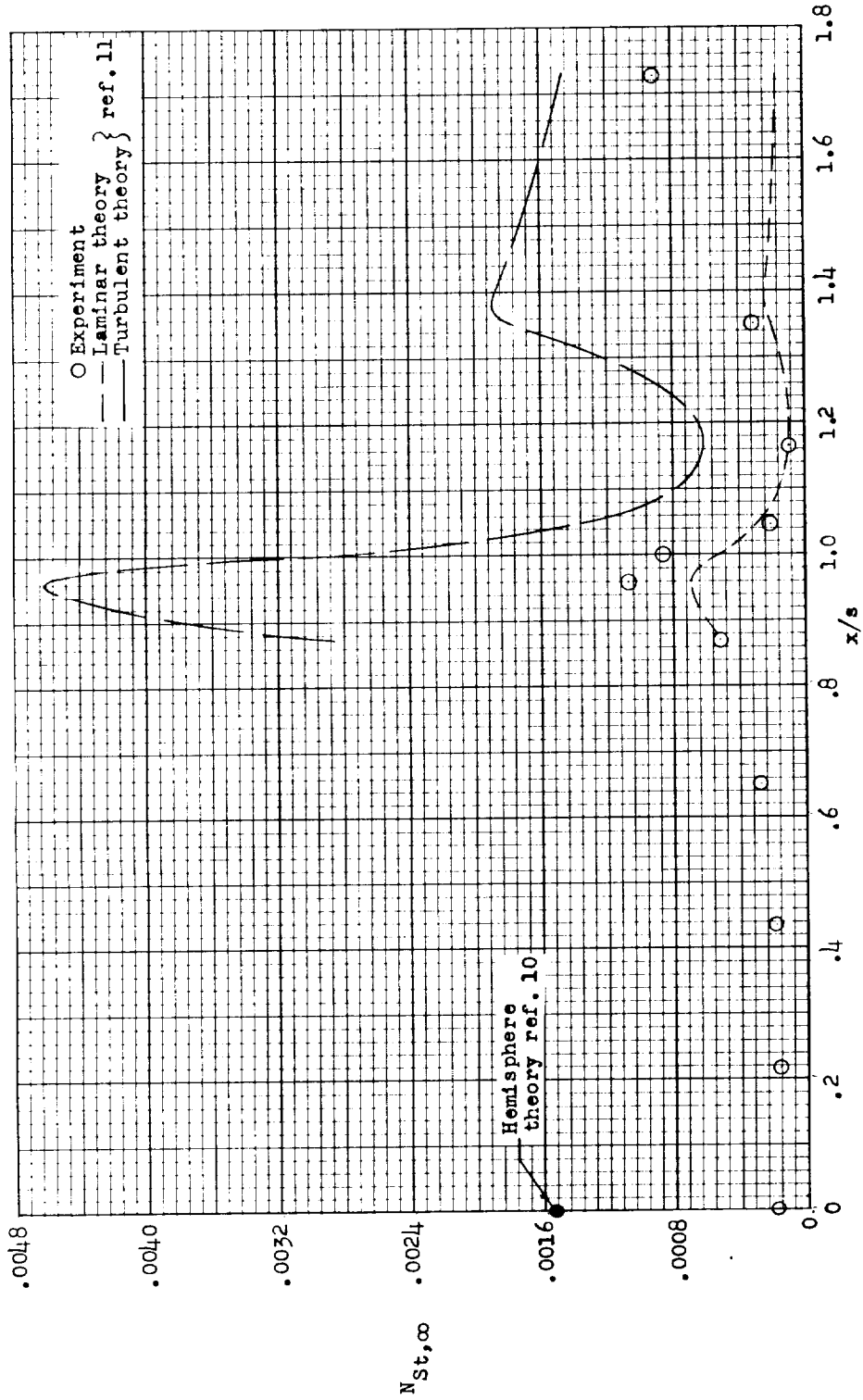
(c) $M_\infty = 6.64$; $t = 6.5$; $R_{\infty,D} = 14 \times 10^6$.

Figure 11.- Continued.
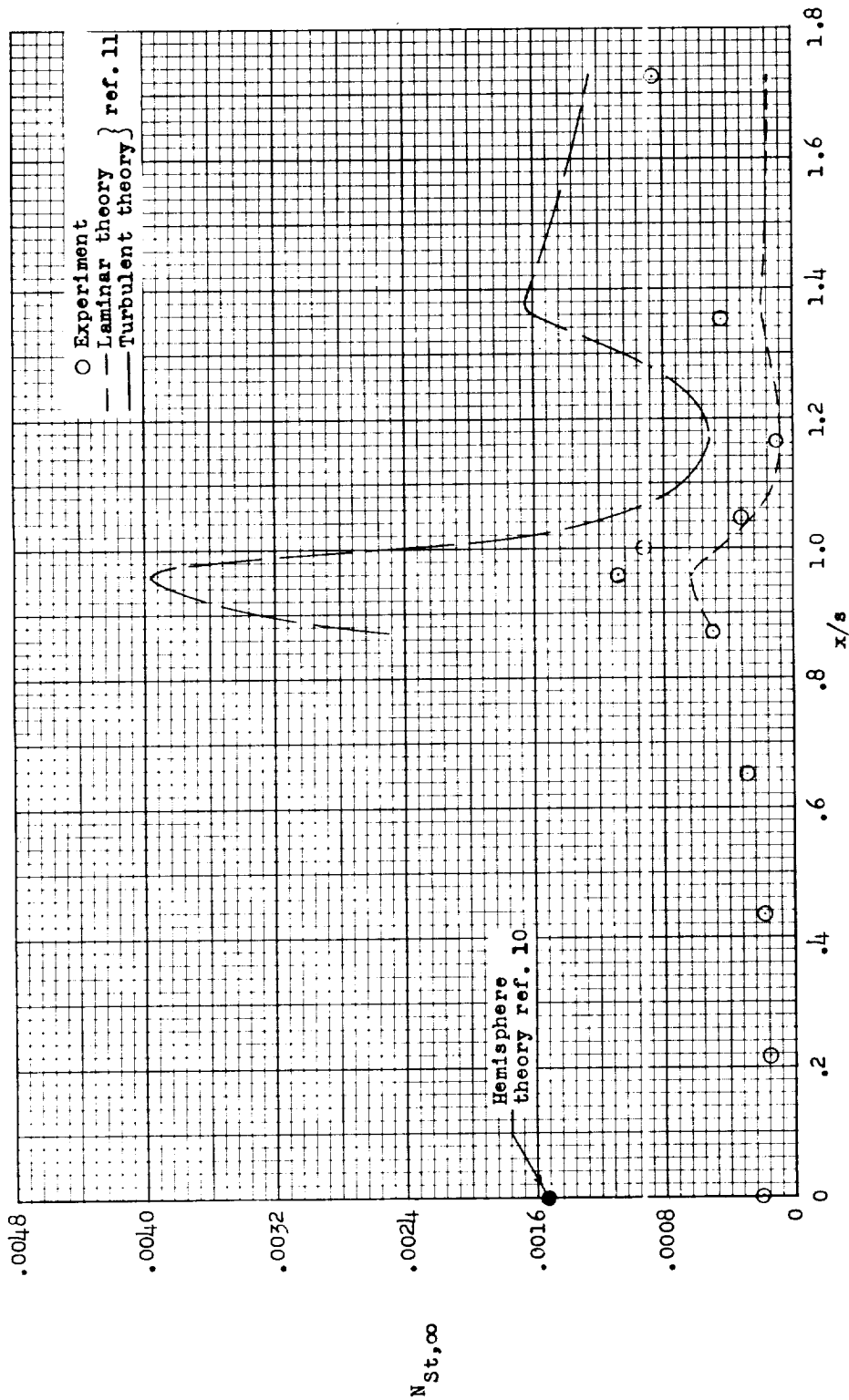
(d) $M_\infty = 6.25$; $t = 6.88$; $R_{\infty,D} = 12.2 \times 10^6$.
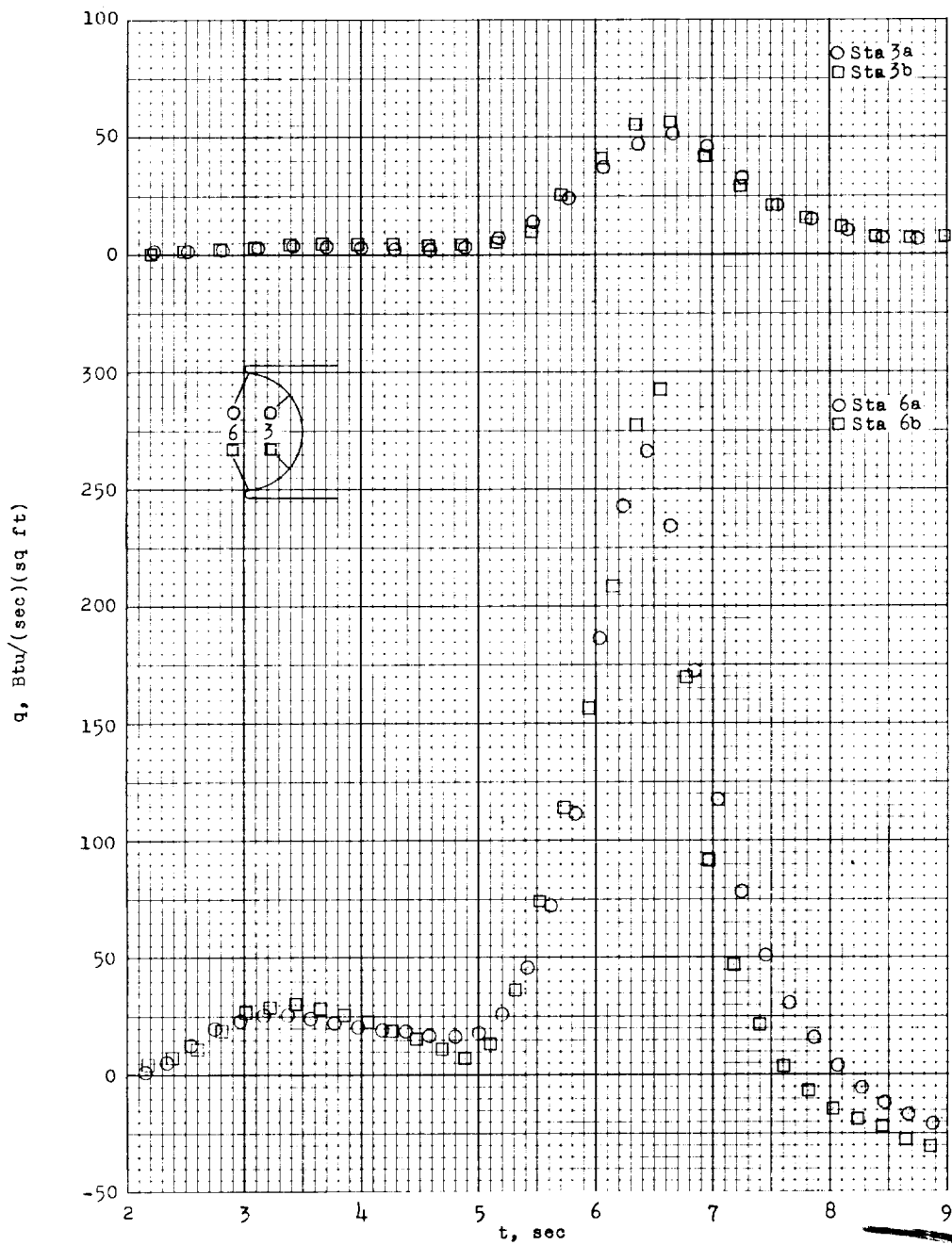
Figure 11.- Continued.
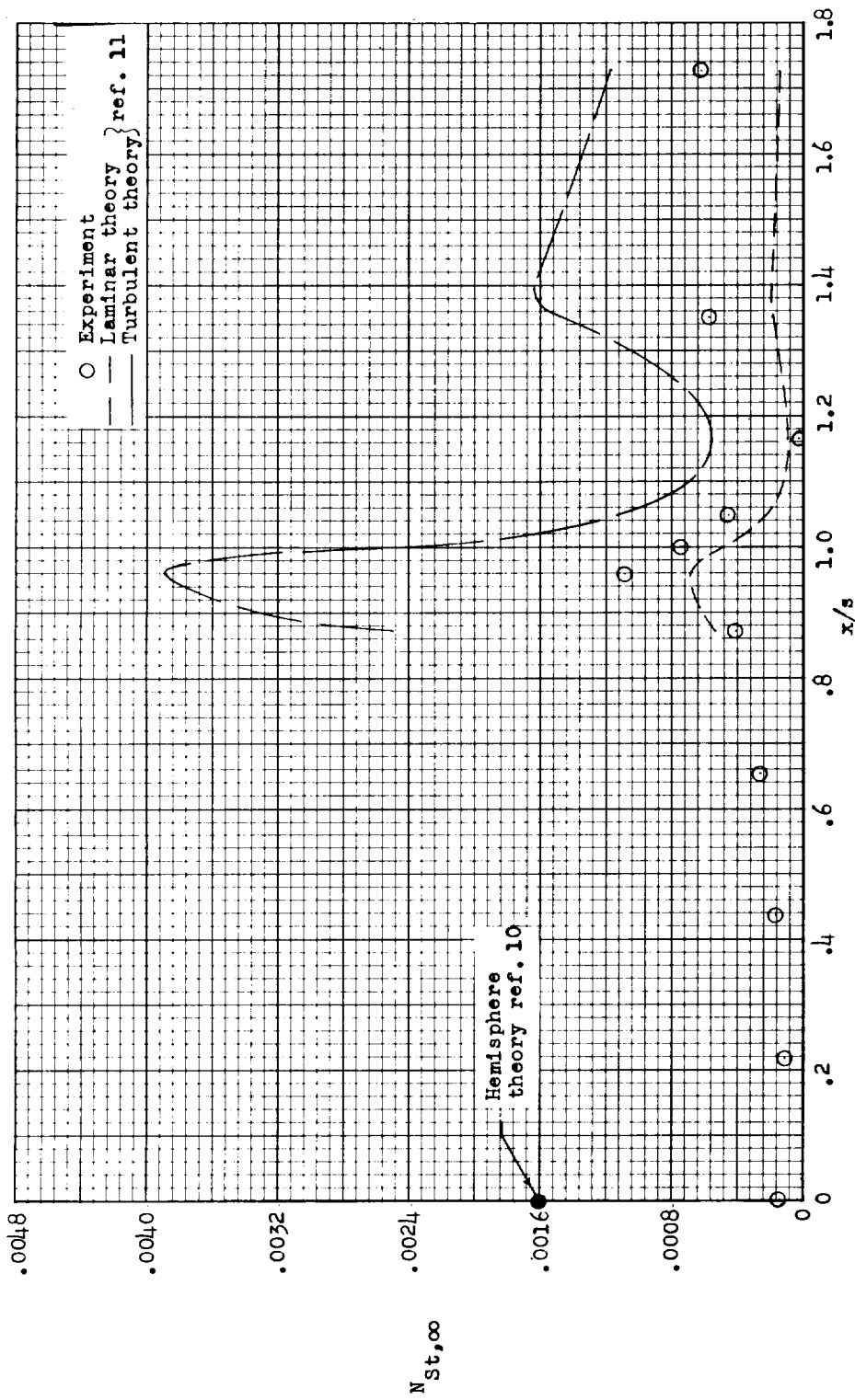
(e) $M_\infty = 5.5$; $t = 7.44$; $R_{\infty,D} = 10.0 \times 10^6$.
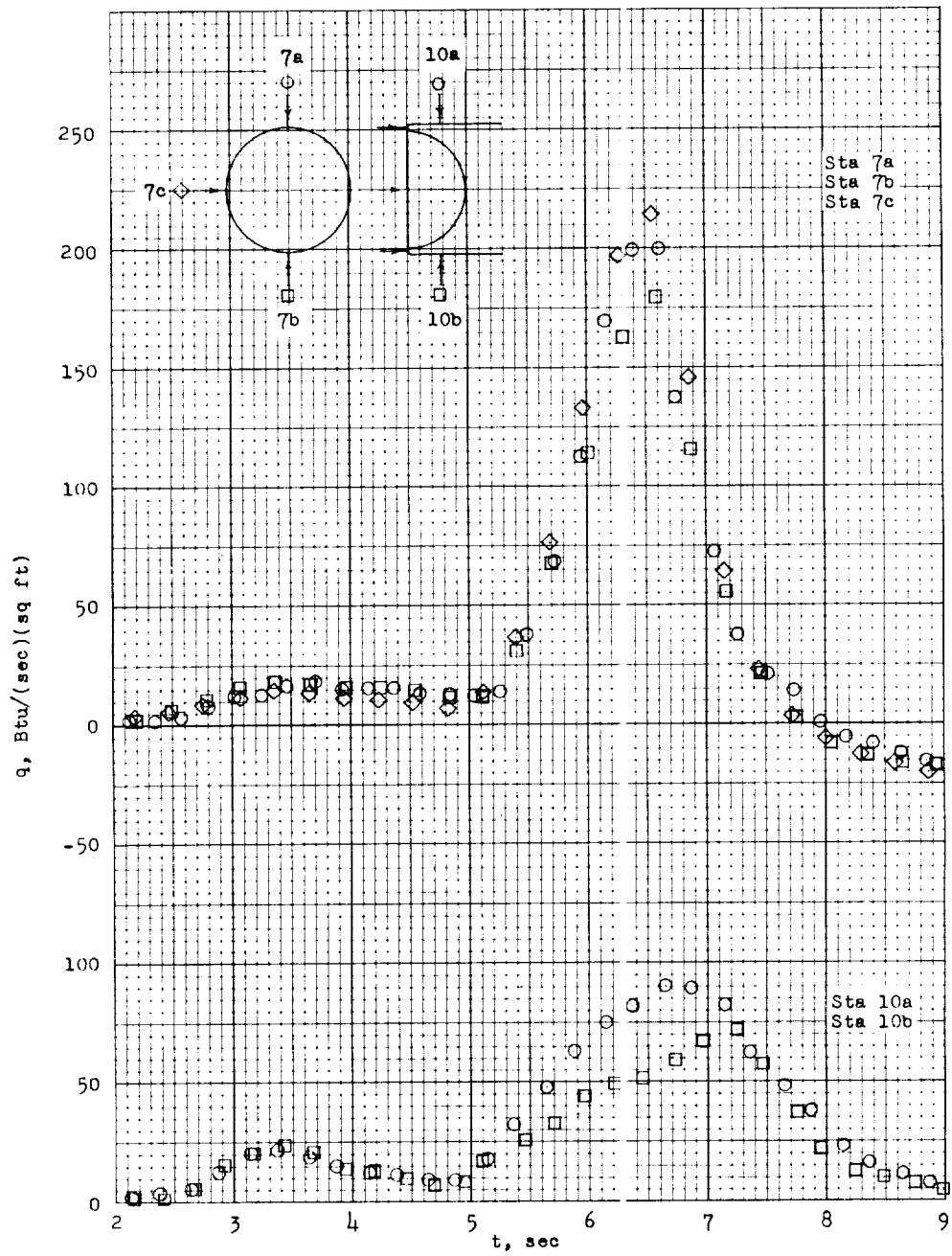
Figure 11.- Continued.
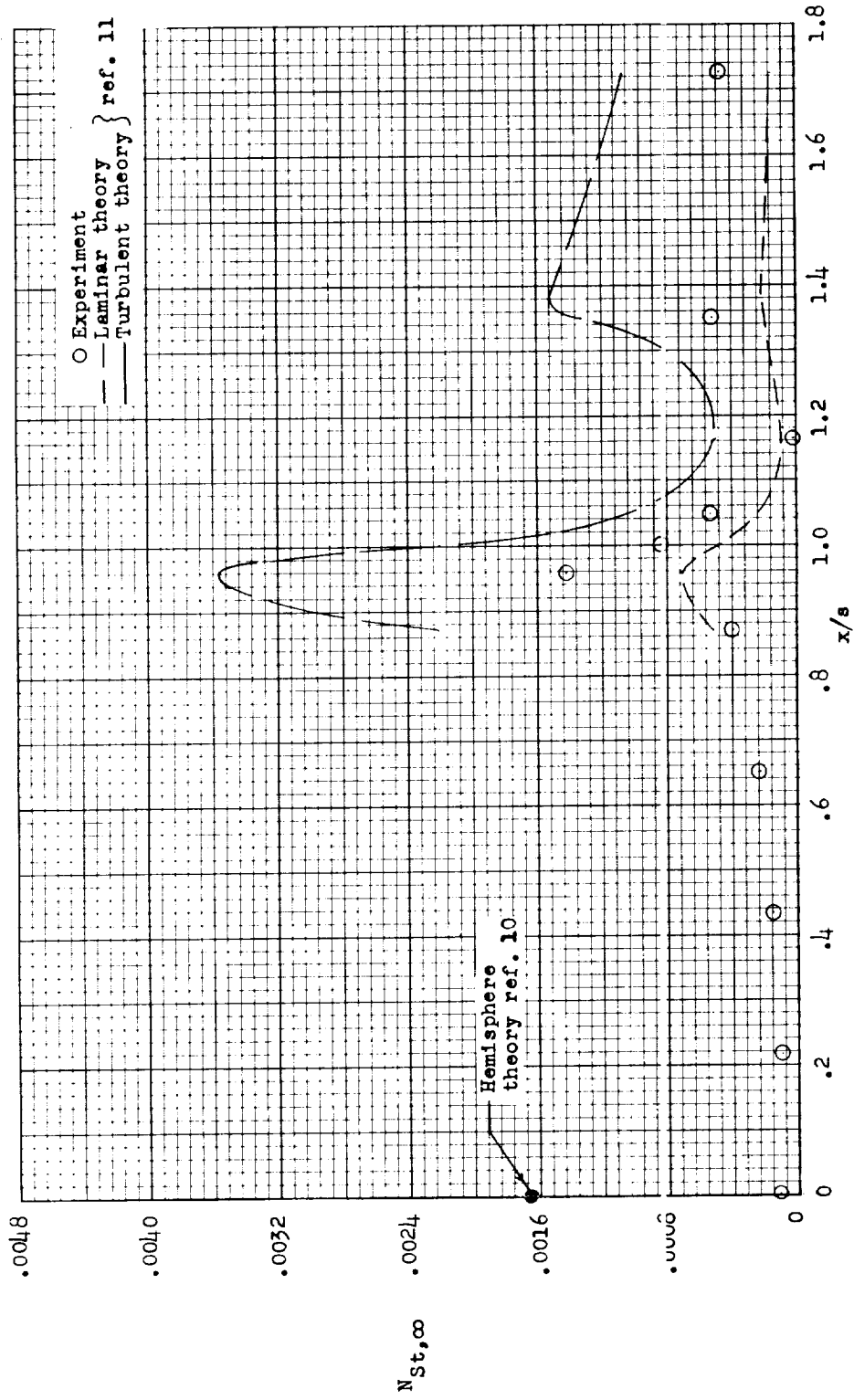
(f) $M_\infty = 4.75$; $t = 8.15$; $R_{\infty,D} = 7.9 \times 10^6$.

Figure 11.- Concluded.

(a) Stations 3a and 3b inside the cup and stations 6a and 6b
just inside the lip of the cup.

Figure 12.- Comparison of one-dimensional heating rates at symmetrical
stations.

(b) Stations 7a, 7b, and 7c on the lip and stations 10a and 10b
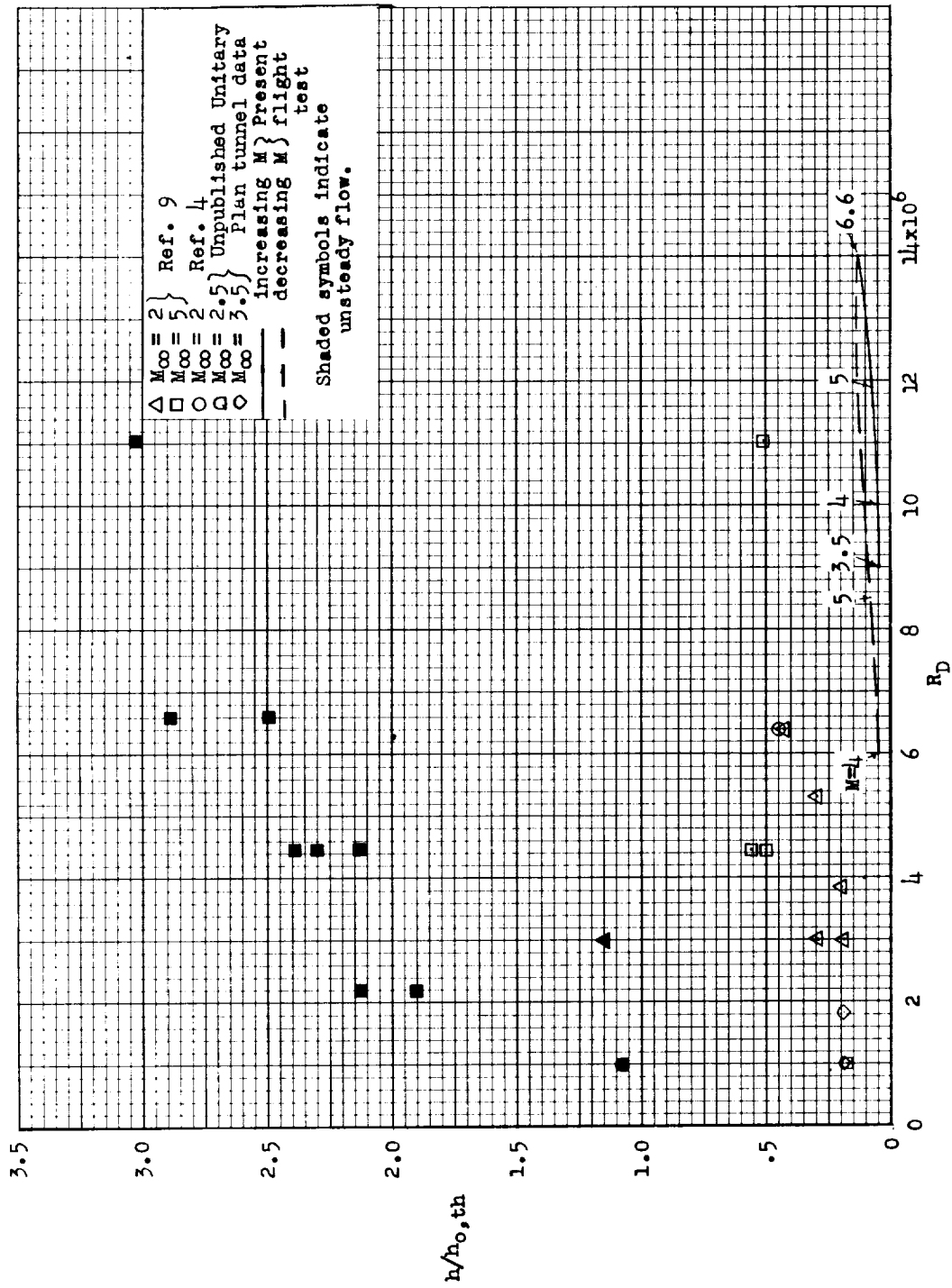on the cylinder.

Figure 12.- Concluded.

Figure 13.- Comparison of results at the stagnation point of a cup nose in terms of theoretical hemispherical stagnation-point heating.